

NPS-ME-01-003

# NAVAL POSTGRADUATE SCHOOL

## Monterey, California



**MODELING THE BIODYNAMICAL RESPONSE OF  
THE HUMAN THORAX WITH BODY ARMOR  
FROM A BULLET IMPACT**

by

John A. Lobuono  
and  
Young W. Kwon

July 2000 – March 2001

Approved for public release; distribution is unlimited.

Prepared for:  
Armed Forces Institute of Pathology  
14<sup>th</sup> and Alaska, NW  
Washington, DC 20306-6000

NAVAL POSTGRADUATE SCHOOL  
Monterey, California 93943

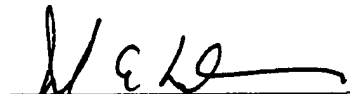
RADM DAVID R. ELLISON  
Superintendent


R. S. ELSTER  
Provost

This technical report was prepared in conjunction with research sponsored in part by Armed Forces Institute of Pathology, Washington DC.


Reproduction of all or part of this report is authorized.

This report was prepared by:


  
JOHN A. LOBUONO  
Lieutenant, United States Navy

  
YOUNG W. KWON  
Professor of Mechanical Engineering

Reviewed by:

  
TERRY R. MCNELLEY,  
Chairman  
Department of Mechanical Engineering

Released by:

  
DAVID W. NETZER  
Associate Provost and  
Dean of Research

REPORT DOCUMENTATION PAGE			Form Approved OMB No. 0704-0188
Public reporting burden for this collection of information is estimated to average 1 hour per response, including the time for reviewing instruction, searching existing data sources, gathering and maintaining the data needed, and completing and reviewing the collection of information. Send comments regarding this burden estimate or any other aspect of this collection of information, including suggestions for reducing this burden, to Washington headquarters Services, Directorate for Information Operations and Reports, 1215 Jefferson Davis Highway, Suite 1204, Arlington, VA 22202-4302, and to the Office of Management and Budget, Paperwork Reduction Project (0704-0188) Washington DC 20503.			
1. AGENCY USE ONLY (Leave blank)	2. REPORT DATE March 2001	3. REPORT TYPE AND DATES COVERED Technical Report	
4. TITLE AND SUBTITLE: Title (Mix case letters) Modeling the Biodynamical Response of the Human Thorax with Body Armor from a Bullet Impact		5. FUNDING NUMBERS  MIPR0LNPS7045 1	
6. AUTHOR(S) Lobo John A.		8. PERFORMING ORGANIZATION REPORT NUMBER NPS-ME-01-003	
7. PERFORMING ORGANIZATION NAME(S) AND ADDRESS(ES) Naval Postgraduate School Monterey, CA 93943-5000		10. SPONSORING/ MONITORING AGENCY REPORT NUMBER	
9. SPONSORING/ MONITORING AGENCY NAME(S) AND ADDRESS(ES) Armed Forces Institute of Pathology, 14th and Alaska, NW, Washington, DC 20306-6000		10. SPONSORING/ MONITORING AGENCY REPORT NUMBER	
11. SUPPLEMENTARY NOTES The views expressed in this thesis are those of the author and do not reflect the official policy or position of the Department of Defense or the U.S. Government.			
12a. DISTRIBUTION/ AVAILABILITY STATEMENT Approved for public release; distribution is unlimited		12b. DISTRIBUTION CODE A	
13. ABSTRACT (maximum 200 words)  The objective of this study is to develop a finite element model of the human thorax with a protective body armor system so that the model can adequately determine the thorax's biodynamical response from a projectile impact. The finite element model of the human thorax consists of the thoracic skeleton, heart, lungs, major arteries, major veins, trachea, and bronchi. The finite element model of the human thorax is validated by comparing the model's results to experimental data obtained from cadavers wearing a protective body armor system undergoing a projectile impact. When the model is deemed valid, a parametric study is performed to determine the components of the model that have the greatest effect on its biodynamical response to a projectile impact			
14. SUBJECT TERMS Finite Element Analysis, Human Thorax Model, Impact Analysis, Body Armor			15. NUMBER OF PAGES 79
			16. PRICE CODE
17. SECURITY CLASSIFICATION OF REPORT Unclassified	18. SECURITY CLASSIFICATION OF THIS PAGE Unclassified	19. SECURITY CLASSIFICATION OF ABSTRACT Unclassified	20. LIMITATION OF ABSTRACT UL

SN 7540-01-280-5500

Standard Form 298 (Rev. 2-89)  
Prescribed by ANSI Std. Z39-18

**THIS PAGE INTENTIONALLY LEFT BLANK**

## **ABSTRACT**

The objective of this study is to develop a finite element model of the human thorax with a protective body armor system so that the model can adequately determine the thorax's biodynamical response from a projectile impact. The finite element model of the human thorax consists of the thoracic skeleton, heart, lungs, major arteries, major veins, trachea, and bronchi. The finite element model of the human thorax is validated by comparing the model's results to experimental data obtained from cadavers wearing a protective body armor system undergoing a projectile impact. When the model is deemed valid, a parametric study is performed to determine the components of the model that have the greatest effect on its biodynamical response to a projectile impact.

**THIS PAGE INTENTIONALLY LEFT BLANK**

## TABLE OF CONTENTS

I.	INTRODUCTION .....	1
II.	BACKGROUND .....	3
	A. HUMAN THORACIC SKELETON .....	3
	B. VISCERA IN THORACIC CAVITY .....	11
	C. LITERATURE SURVEY .....	16
III.	FINITE ELEMENT MODEL .....	21
	A. HUMAN THORACIC MODEL .....	21
	1. Modeling of the Thoracic Skeleton .....	22
	2. Modeling of the Viscera in the Human Thorax .....	25
	B. ARMOR .....	28
	C. INTERFACE ELEMENTS .....	29
	D. PROJECTILE .....	29
	E. BOUNDARY CONDITIONS .....	29
	F. MATERIAL PROPERTIES .....	30
III.	RESULTS AND DISCUSSION .....	35
	A. VIABILITY STUDY .....	36
	1. Human Thorax Model with Kevlar and Boron Carbide Plate Body Armor System Struck by NATO 7.62mm Ball MSO Round .....	36
	2. Human Thorax Model with Kevlar Body Armor Struck by a NATO 9mm Full Metal Jacket Round .....	45
	B. PARAMETRIC STUDY .....	53
IV.	CONCLUSIONS AND RECOMMENDATIONS .....	75
	A. CONCLUSIONS .....	75
	B. RECOMMENDATIONS .....	76
	LIST OF REFERENCES .....	77
	INITIAL DISTRIBUTION LIST .....	79

THIS PAGE INTENTIONALLY LEFT BLANK



## LIST OF FIGURES

Figure 1. Coastal Cartilages and Sternum. From Ref. [1] .....	4
Figure 2. Vertebral Column. From Ref. [1] .....	5
Figure 3. Lumbar Vertebra. From Ref. [13] .....	5
Figure 4. Cervical Vertebra. From Ref. [13] .....	5
Figure 5. Thoracic Vertebra (Superior and Lateral Aspects). From Ref. [13] .....	6
Figure 6. Ninth, Tenth, and Eleventh Vertebrae. From Ref. [1] .....	7
Figure 7. (a) Fifth Rib, Inferior Aspect; (b) Fifth Rib, Posterior Aspect; (c) First Rib. From Ref. [13] .....	8
Figure 8. Posterior Aspect of the Sternum. From Ref. [2] .....	10
Figure 9. Cross Sectional View of the Thorax. From Ref. [2] .....	11
Figure 10. Outer Surface of the Left Lung (Upper Figure) and Outer Surface of the Right Lung (Lower Figure). From Ref. [1] .....	13
Figure 11. Trachea and Bronchi. From Ref. [2] .....	14
Figure 12. The Right Side of the Heart with the Wall of the Atrium and Ventricle Cut Away. From Ref. [13] .....	15
Figure 13. Anterior View of the Human Thorax .....	21
Figure 14. Medial View of the Ribs and Spine. From Ref. [12] .....	23
Figure 15. Anterior View of the Sternum. From Ref. [12] .....	23
Figure 16. Muscle on the Thoracic Skeleton. From Ref. [12] .....	24
Figure 17. Articular Cartilage Connecting Sternum and Ribs. From Ref. [12] .....	25
Figure 18. Anterior View of the Lungs .....	26
Figure 19. Anterior View of the Heart .....	27
Figure 20. Kevlar Vest Overlaying the Thoracic Muscle. From Ref. [12] .....	28
Figure 21. Medial View of the Projectile Attached to Kevlar and Boron Carbide Plate Body Armor System. From Ref. [12] .....	30
Figure 22. Load-Elongation Curve for a Rabbit Lamb Tendon Bought to Failure with Constant Rate of Elongation. From Ref. [15] .....	31
Figure 23. Sternum Acceleration (Kevlar and Boron Carbide). After Ref. [13] .....	37
Figure 24. Sternum Velocity (Kevlar and Boron Carbide). After Ref. [13] .....	38
Figure 25. Sternum Displacements (Kevlar and Boron Carbide). After Ref. [13] .....	39
Figure 26. Spinal Acceleration (Kevlar and Boron Carbide). After Ref. [13] .....	40
Figure 27. Spinal Velocity (Kevlar and Boron Carbide). After Ref. [13] .....	41
Figure 28. Spinal Displacement (Kevlar and Boron Carbide). After Ref. [13] .....	41
Figure 29. Pulmonary Artery Acceleration (Kevlar and Boron Carbide). After Ref. [13] ...	42
Figure 30. Trachea Acceleration (Kevlar and Boron Carbide). After Ref. [13] .....	43
Figure 31. Ventricle Pressure Element 215 (Kevlar and Boron Carbide). After Ref. [13] ...	44
Figure 32. Ventricle Pressure Element 193 (Kevlar and Boron Carbide). After Ref. [13] ...	44
Figure 33. Sternum Acceleration (Kevlar). After Ref. [13] .....	46
Figure 34. Sternum Velocity (Kevlar). After Ref. [13] .....	46
Figure 35. Sternum Displacement (Kevlar). After Ref. [13] .....	47
Figure 36. Spinal Acceleration (Kevlar). After Ref. [13] .....	49

Figure 37. Spinal Velocity (Kevlar). After Ref. [13].	49
Figure 38. Spinal Displacement (Kevlar). After Ref. [13]	50
Figure 39. Pulmonary Acceleration (Kevlar). After Ref. [13].	51
Figure 40. Ventricle Pressure (Kevlar). After Ref. [13]	52
Figure 41. Pulmonary Acceleration (Kevlar and Boron Carbide Armor with Stiffness of Springs Decreased by a Factor of 10).After Ref. [13].	54
Figure 42. Ventricle Pressure Element 193 (Kevlar and Boron Carbide Armor with Stiffness of Springs Decreased by a Factor of 10). After Ref. [13].	55
Figure 43. Ventricle Pressure Element 215 (Kevlar and Boron Carbide Armor with Stiffness of Springs Decreased by a Factor of 10). After Ref. [13].	55
Figure 44. Sternum Acceleration (Kevlar and Boron Carbide Armor with Stiffness of Springs Decreased by a Factor of 10). After Ref. [13].	56
Figure 45. Spinal Acceleration (Kevlar and Boron Carbide Armor with Stiffness of Springs Decreased by a Factor of 10).After Ref. [13].	56
Figure 46. Pulmonary Acceleration (Kevlar and Boron Carbide Armor with Stiffness of Springs Increased by a Factor of 10). After Ref. [13]	57
Figure 47. Ventricle Pressure Element 193 (Kevlar and Boron Carbide Armor with Stiffness of Springs Increased by a Factor of 10). After Ref. [13].	58
Figure 48. Ventricle Pressure Element 215 (Kevlar and Boron Carbide Armor with Stiffness of Springs Increased by a Factor of 10).After Ref. [13].	58
Figure 49. Sternum Acceleration (Kevlar and Boron Carbide Armor with Stiffness of Springs Increased by a Factor of 10). After Ref. [13]	59
Figure 50. Spinal Acceleration (Kevlar and Boron Carbide Armor with Stiffness of Springs Increased by a Factor of 10). After Ref. [13]	59
Figure 51. Sternum Acceleration (Kevlar and Boron Carbide Armor with Young's Modulus of Pericardium Decreased by a Factor of 10). After Ref. [13]	61
Figure 52. Spinal Acceleration (Kevlar and Boron Carbide Armor with Young's Modulus of Pericardium Decreased by a Factor of 10).After Ref. [13]	62
Figure 53. Pulmonary Artery Acceleration (Kevlar and Boron Carbide Armor with Young's Modulus of Pericardium Decreased by a Factor of 10). After Ref. [13].	62
Figure 54. Ventricle Pressure Element 193 (Kevlar and Boron Carbide Armor with Young's Modulus of Pericardium Decreased by a Factor of 10). After Ref. [13].	63
Figure 55. Ventricle Pressure Element 215 (Kevlar and Boron Carbide Armor with Young's Modulus of Pericardium Decreased by a Factor of 10). After Ref. [13].	63
Figure 56. Sternum Acceleration (Kevlar and Boron Carbide Armor with Young's Modulus of Pericardium Increased by a Factor of 10). After Ref. [13]	64
Figure 57. Spinal Acceleration (Kevlar and Boron Carbide Armor with Young's Modulus of Pericardium Increased by a Factor of 10). After Ref. [13].	64
Figure 58. Pulmonary Artery Acceleration (Kevlar and Boron Carbide Armor with Young's Modulus of Pericardium Increased by a Factor of 10). After Ref. [13].	65

Figure 59.	Ventricle Pressure Element 193 (Kevlar and Boron Carbide Armor with Young's Modulus of Pericardium Increased by a Factor of 10). After Ref. [13].	65
Figure 60.	Ventricle Pressure Element 215 (Kevlar and Boron Carbide Armor with Young's Modulus of Pericardium Increased by a Factor of 10). After Ref. [13].	66
Figure 61.	Spinal Acceleration (Kevlar and Boron Carbide Armor with Stiffness of Springs Between Heart Lungs Decreased by a Factor of 10). After Ref. [13].	67
Figure 62.	Pulmonary Artery Acceleration (Kevlar and Boron Carbide Armor with Stiffness of Springs Between Heart Lungs Decreased by a Factor of 10). After Ref. [13].	67
Figure 63.	Ventricle Pressure Element 193 (Kevlar and Boron Carbide Armor with Stiffness of Springs Between Heart Lungs Decreased by a Factor of 10). After Ref. [13].	68
Figure 64.	Ventricle Pressure Element 215 (Kevlar and Boron Carbide Armor with Stiffness of Springs Between Heart Lungs Decreased by a Factor of 10). After Ref. [13].	68
Figure 65.	Spinal Acceleration (Kevlar and Boron Carbide Armor with Stiffness of Springs Between Heart Lungs Increased by a Factor of 10). After Ref. [13].	69
Figure 66.	Pulmonary Artery Acceleration (Kevlar and Boron Carbide Armor with Stiffness of Springs Between Heart Lungs Increased by a Factor of 10). After Ref. [13].	69
Figure 67.	Ventricle Pressure Element 193 (Kevlar and Boron Carbide Armor with Stiffness of Springs Between Heart Lungs Increased by a Factor of 10). After Ref. [13].	70
Figure 68.	Ventricle Pressure Element 215 (Kevlar and Boron Carbide Armor with Stiffness of Springs Between Heart Lungs Increased by a Factor of 10). After Ref. [13].	70
Figure 69.	Trachea Acceleration (Kevlar and Boron Carbide Armor with Young's Modulus of Trachea Increased by a Factor of 10). After Ref. [13].	72
Figure 70.	Pulmonary Artery Acceleration (Kevlar and Boron Carbide Armor with Young's Modulus of Pulmonary Artery Increased by a Factor of 10). After Ref. [13].	72
Figure 71.	Trachea Acceleration (Kevlar and Boron Carbide Armor with Young's Modulus of Trachea Decreased by a Factor of 10). After Ref. [13].	73
Figure 72.	Pulmonary Artery Acceleration (Kevlar and Boron Carbide Armor with Young's Modulus of Pulmonary Artery Decreased by a Factor of 10). After Ref. [13].	73

THIS **PAGE** INTENTIONALLY LEFT BLANK

## LIST OF TABLES

Table 1. Material Properties of the <b>Human</b> Thorax .....	33
Table 1. Material Properties of Human Thorax (cont.) .....	<b>34</b>

THIS **PAGE** INTENTIONALLY LEFT BLANK

## I. INTRODUCTION

The study of protective body armor systems has taken on a great importance due to our military forces performing peacekeeping missions such as in Kosovo. The Army has worn 'Flak' jackets for some time during their missions. A protective body armor system is required to provide personnel protection against any possible threats such as enemy fire and shrapnel. The protective body armor system must provide resistance against projectile penetration and prevent the projectile's force causing significant or lethal injuries to the human body that would prevent personnel from performing their mission.

The purpose of this research is to develop a finite element model of the human thorax with a protective body armor system so that the model adequately determines the biodynamical response of the thorax to a projectile impact. The biodynamical response of the human thorax is examined under two different scenarios. The first case studies the biodynamical response of the human thorax and with body armor consisting of Kevlar sheet and a Boron Carbide plate struck by a **NATO 7.62 mm M80** ball. The second case studies the biodynamical response of the human thorax with body armor consisting of a Kevlar sheet struck by a **NATO 9mm** round. The finite element model of the human thorax consists of the thoracic skeleton, heart, lungs, major arteries, major veins, trachea, and bronchi. The finite element model is designed to determine the acceleration of the spine, sternum, pulmonary artery, and trachea, velocity and displacement of the spine and sternum, and ventricle pressure. The finite element model is validated by comparing its results to experimental data collected from cadavers. When the finite element model is

determined to be valid, a parametric study is conducted to determine the essential components of the model.

With the development of the finite element model of the human thorax, the model can be used to determine the biodynamical response of the human thorax to different types of projectiles using different protective body armor systems. Knowing the biodynamical response to projectile impact, additional body armor systems can be developed to reduce the seriousness of an injury from being struck by a projectile. The finite element model will also reduce the dependence on costly experimentation with cadavers for projectile analysis thus providing an economical alternative.



## **II. BACKGROUND**

The human thoracic skeleton and the viscera in the thoracic cavity will be discussed to provide an understanding of the parts of the human thorax that are modeled. Also the discussion of the human thorax will provide the rationale of how the components are modeled in the finite element model of the thorax.

### **A. HUMAN THORACIC SKELETON**

The human thorax is an osteo-cartilaginous cage that contains and protects the major organs of respiration and circulation. The twelve dorsal vertebrae and the posterior portion of the ribs form the posterior surface of the thorax. The anterior surface of the thorax consists of the sternum and costal cartilages. The lateral surfaces of the thorax consist of the ribs. The upper opening of the thorax is formed by the first rib, first dorsal vertebrae, and the upper portion of the sternum. The lower opening of the thorax is formed by the twelfth dorsal vertebrae, twelfth rib, the subcostal angle formed by the seventh, eighth, ninth, tenth, and eleventh ribs, and the diaphragm. The anterior view of the thorax illustrating the sternum and costal cartilages is shown in Figure 1. [Refs. 1 & 2]

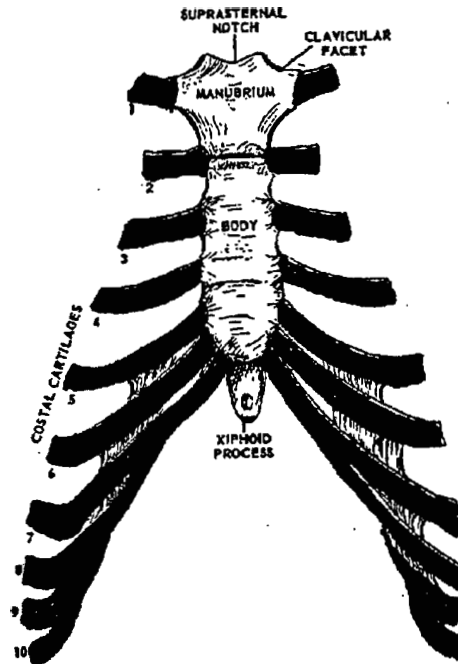


Figure 1. Costal Cartilages and Sternum. From Ref. [1].

The function of the spine is to support the head and trunk and protect the spinal cord. The spine is composed of 33 vertebrae, 23 discs, and connecting ligaments. The spine consists of five regions, cervical, dorsal (thoracic), lumbar, sacral, and coccygeal. The names of each vertebra is based on the region of the spine the vertebra is located. Seven vertebrae are located in the cervical region, twelve in the dorsal region, five in the lumbar region, five in the sacral region and four in the coccygeal region. The vertebrae in the cervical, dorsal and lumbar regions of the spine are separated throughout life. The vertebrae in the sacral and coccygeal region fuse together to form the sacrum and coccyx. The spinal column, lumbar vertebra, and a cervical vertebra are shown respectively in Figure 2, 3, and 4. [Refs. 7 & 8]

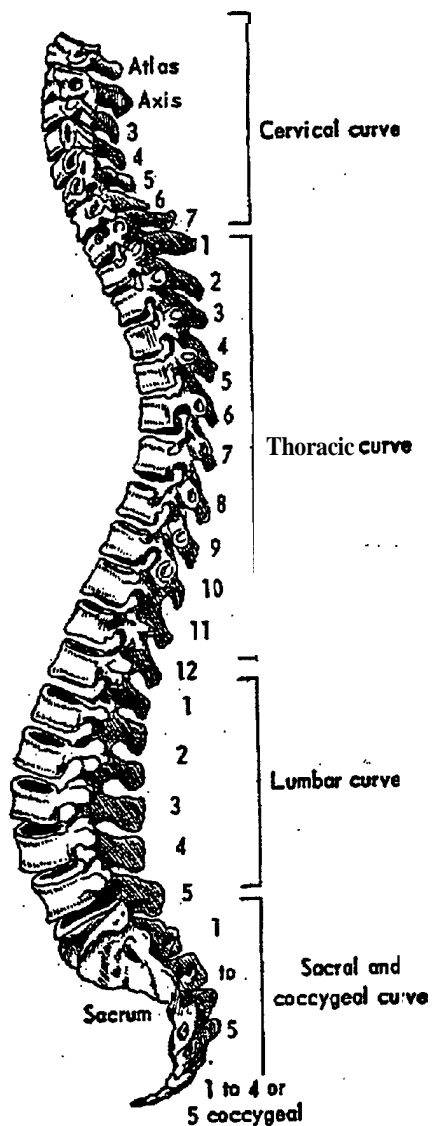


Figure 2. Vertebral Column. From Ref. [1].

A typical vertebra is composed of two principal parts, a body and a vertebral arch as shown in Figure 5. The body is a thick disc-like mass of cancellous bone with a thin covering of compact bone situated anteriorly to the spinal cord. The body is convex horizontally in front and concave behind and forms one side of the spinal canal. The vertebral bodies lie upon each other like a vertical column with a disc of fibrous cartilage

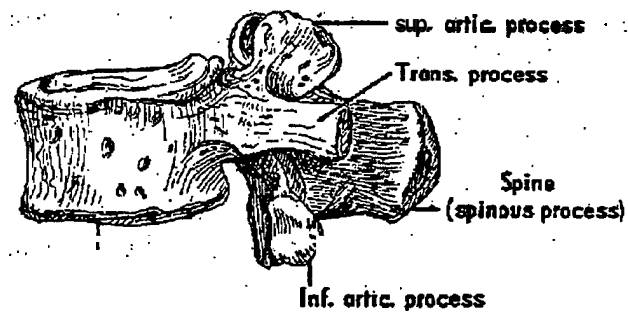


Figure 3. Lumbar Vertebra. From Ref. [1].

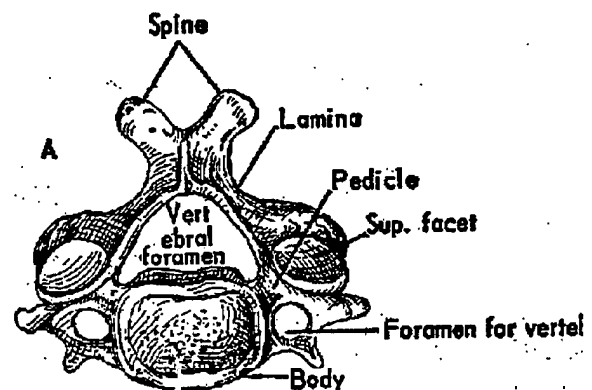


Figure 4. Cervical Vertebra. From Ref. [13].

between each adjacent vertebra to form the vertebral column as shown in Figure 6. The vertebral arch is a ring of bone that is located posteriorly of the body and forms the other side of the spinal canal. The space that is enclosed by the body and the vertebral arch is the vertebral foramen. The vertebral arch consists of two pedicles, two laminae, a spinous process, two transverse processes, and four articular processes to allow interaction with the neighboring vertebrae. The pedicles are two angled bars of bone that sprout posteriorly from the body. The laminae are a pair of broad plates that extend from the pedicles and meet and fuse in the midline, posterior from the center of the body. At the point of fusion, the spinous process is formed and points backward and downwards. The transverse process protrudes laterally and posteriorly on each side of the junction between the laminae and the pedicle. The articular processes are also pointed in this direction. The articular processes consist of two pairs, an inferior and superior. The superior articular processes face backward and the inferior articular processes face forward. The superior articular process of the lower vertebrae and the inferior articular process of the upper vertebrae interact to provide stability of the spine. [Refs. 1 & 2]

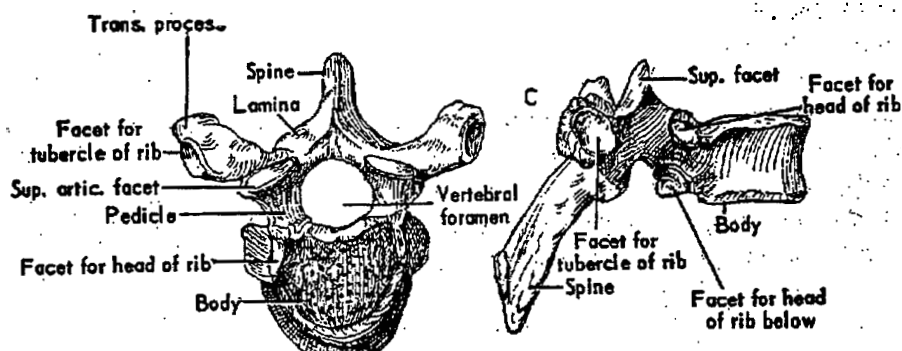


Figure 5. Thoracic Vertebra (Superior and Lateral Aspects). From Ref. [13]

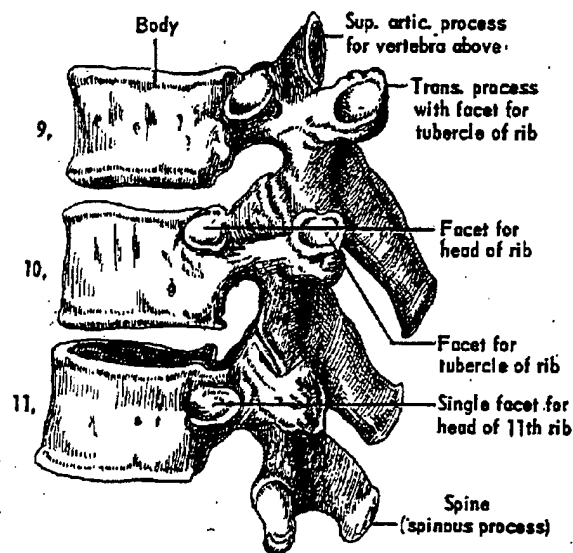


Figure 6. Ninth, Tenth, and Eleventh Vertebrae. From Ref. [1]

The ribs are arched bones. Twenty-four ribs in twelve pairs form the major parts of the thoracic wall. The ribs are numbered in ascending order with the most superior rib being numbered as the first rib. The first seven ribs, called the true ribs, are connected directly to the sternum. The remaining ribs eight through twelve are called the false ribs. Ribs eight through ten are connected to the cartilage of the ribs above. The floating ribs, ribs eleven and twelve are free at the anterior ends. The ribs vary in direction and length. The upper ribs compared to the lower ribs are less oblique. The length of the ribs increase from the first to the seventh rib and then the length of the ribs start to decrease to the twelfth rib. [Refs 1 & 2]

Each rib consists of two extremities, posterior (vertebral) and anterior (sternal) with the body of the rib called the shaft as shown in Figure 7. The posterior (vertebral) end consists of a head, neck, and tuberosity. The head consists of two facets that are separated by a ridge. The facets articulate with the costal cavity formed by two adjacent

vertebrae. The ridge attaches to the intervertebral disc through the interarticular ligament. The neck extends from the head to the tubersoity. The neck is the flattened portion of the rib and provides for attachment of various ligaments. The tubersoity has an articular and nonarticular portion. The articular portion has a small oval surface that articulates with the transverse process of the lower vertebrae. The nonarticular portion provides for ligament attachment. The shaft is thin and flat. The shaft is bent and twisted as it extends from the posterior extremity to the anterior extremity. The bend in the shaft is called the angle. The anterior extremity is flattened with a porous oval depression for attachment of the coastal cartilage. [Refs. 1 & 2]

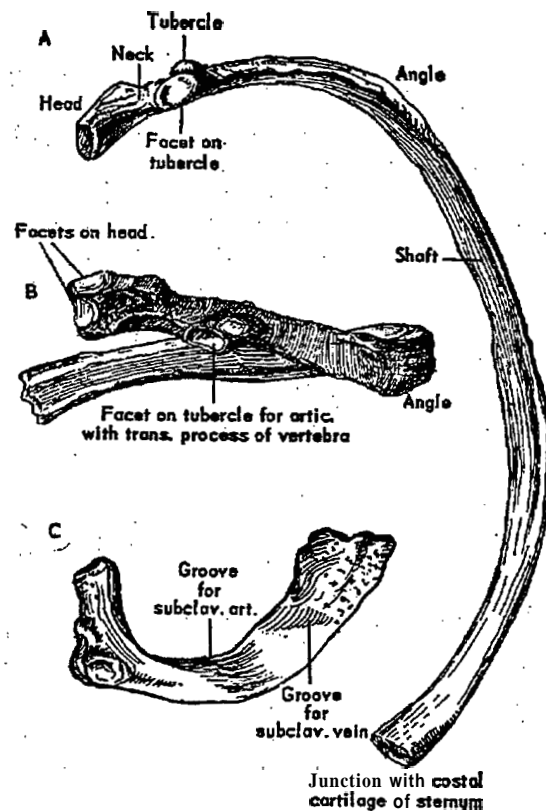


Figure 7. (a) Fifth Rib, Inferior Aspect; (b) Fifth Rib, Posterior Aspect; (c) First Rib. From Ref. [1].

The first, second, tenth, eleventh, and twelfth ribs have some peculiarities compared to the other ribs. The first rib is the shortest and the most curved compared to all the other ribs. The first rib also has only one facet for articulation with the body of a vertebra. The second rib is longer and has a similar shape compared to the first rib. The tenth rib has only a single articulate facet on its head. The eleventh and twelfth ribs have a single articulate facet on their head, no neck or tuberosity and are pointed at their extremities. The eleventh rib has a shaft angle, while the twelfth rib has no angle. [Refs. 1 & 2]

The sternum is a flat thin bone in the median of the front of the chest. The sternum consists of three parts, manubrium, gladiolus and the ensiform (xiphoid appendix) as shown in Figure 8. The manubrium is the upper portion of the sternum. The manubrium has a triangular shape where it is broad and thick above and gets narrow as it approaches the gladiolus. The manubrium, at its lateral margin, has facets for the reception of the costal cartilage for the first and part of the second rib pairs. The gladiolus is the middle portion of the sternum and is the largest portion of the sternum. The gladiolus is longer and thinner compared to the manubrium. The gladiolus at its lateral margin contains facets to receive the costal cartilage from parts of the second rib pair and the third through seventh rib pairs. The ensiform is the lower pointed portion of the sternum. The ensiform is the smallest portion of the sternum and it is elongated and thin. The ensiform has a facet to articulate with the lower half of the costal cartilage of the seventh rib. [Refs. 1 & 2]

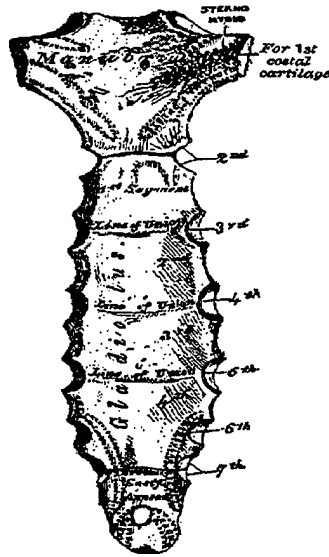


Figure 8. Posterior Aspect of the Sternum. From Ref. [2]

The costal cartilage consists of hyaline cartilage that brings the ribs to the sternum. The costal cartilage's material properties provide flexibility for the thorax. The first seven pairs of costal cartilage connect the first seven pairs of ribs to the sternum. The eighth through the tenth costal cartilages connect to the lower border of costal cartilage of the preceding rib pair. The costal cartilage for the eleventh and twelfth rib pairs is attached to its extremities and does not extend to the sternum. The costal cartilages vary in length, breadth, and direction. The length of the costal cartilage increases in length from the first rib pair to the seventh rib pair and then decreases in length. The costal cartilages also diminish in breadth from the first rib pair to the last rib pair. The outer extremities of the costal cartilage are continuous with the osseous tissue of the rib that it belongs to. The inner extremity of the costal cartilage for the first rib pair is continuous with the sternum. The inner extremities of the costal cartilage for the second thorough seventh rib pairs are articulated into the lateral margins



of the sternum. The inner extremities of the costal cartilage for the eight through tenth **rib** pairs are connected with the cartilage above. The inner extremities of the costal cartilage for the eleventh and twelfth **rib** pairs are free and pointed. [Refs. I & 2]

## B. VISCERA IN THORACIC CAVITY

The thoracic **cavity** is divided into three regions, the two pleura cavities and the mediastinum cavity as shown in Figure 9. The pleura cavities are the regions that occupy the right and left side of the thoracic cavity and where each lung is situated in one of the pleura cavities. The mediastinum is the region in the middle of the thoracic cavity that separates the pleura cavities. The mediastinum extends from the sternum in front to the spine behind and contains all viscera in the thorax except the lungs. [Refs. I & 2]

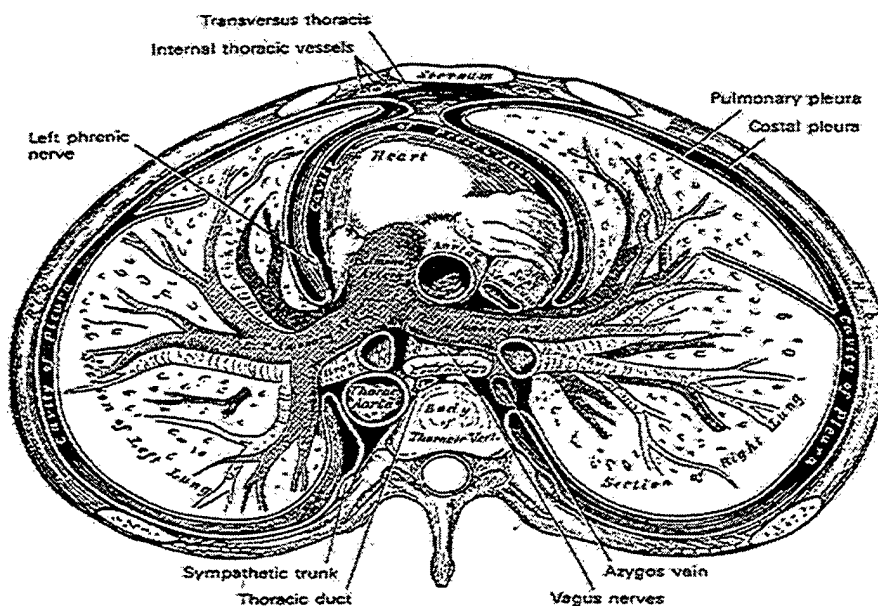


Figure 9. Cross Sectional View of the Thorax, From Ref. [2].

The lungs are the most important organs of respiration. Each lung is conical in shape as shown in Figure 10. The lung's apex extends 1 to 1.5 inches above the first rib pair and its base rests upon the diaphragm. The substance of the lung is a light porous spongy texture that is highly elastic. The left lung is divided into two lobes, an upper and lower by an oblique fissure. The right lung is divided into three lobes, upper, middle, and lower, by the horizontal and oblique fissures. The root of each lung consists of the two pulmonary veins, pulmonary artery, bronchus and bronchial vessels. Each lung is covered by the pleura, which is a serous membrane that covers its exterior surface and encloses the lung up to its root and then reflects upon the thorax's inner surface. The portion of the pleurae that covers the surface of the lung and dips into the fissure between the lobes is the pleura pulmonalis (visceral layer of pleura). The portion of the pleura that covers the inner surface of the thorax is the pleura costalis (partial layer of pleura). The two layers are in contact except for a serous fluid, which allows the layers to glide upon each other. [Refs. 1 & 2]

The trachea and bronchi are the respiratory airways located in the mediastinum. The trachea is a cartilaginous and membranous tube that has a cylindrical shape where it is flattened posteriorly. The trachea extends from the lower part of the larynx, level with the sixth cervical vertebra and extends to the fifth dorsal vertebra where it divides into the left and right bronchi. The right bronchus divides into three branches, which go to the right lung. The left bronchus divides into two branches, which go to the left lung. The right bronchus compared to the left bronchus is shorter, wider, and does not diverge abruptly from the trachea than the left bronchus. However, the left bronchus is nearly

two inches longer in length compared to the right bronchus. The trachea and bronchi are depicted in Figure 11. [Refs. 1 & 2]

The trachea and the right and left bronchi are composed of incomplete rings of cartilage, fibrous tissue, muscular fibers, mucous membrane, and glands. The cartilage forms the anterior two thirds of the circumference of the trachea where the remaining circumference of the trachea is completed by fibrous tissue. [Refs. 1 & 2]

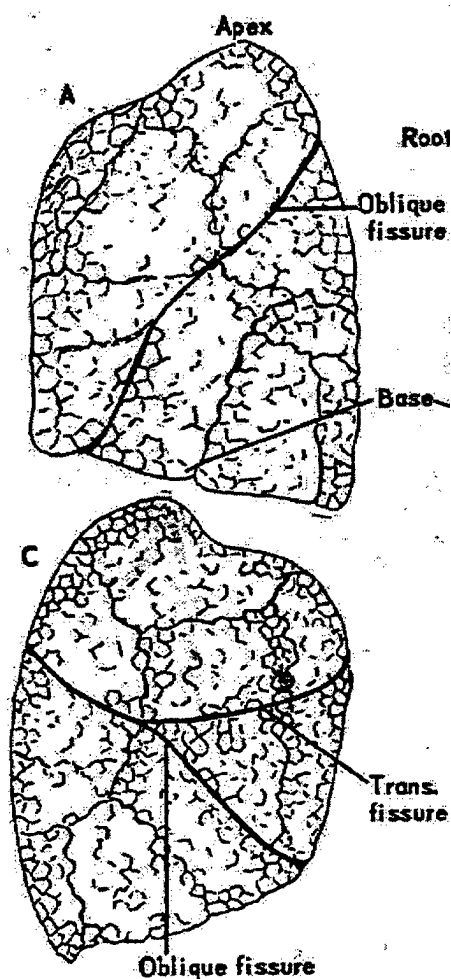


Figure 10. Outer Surface of the Left Lung (Upper Figure) and Outer Surface of the Right Lung (Lower Figure). From Ref. [1]

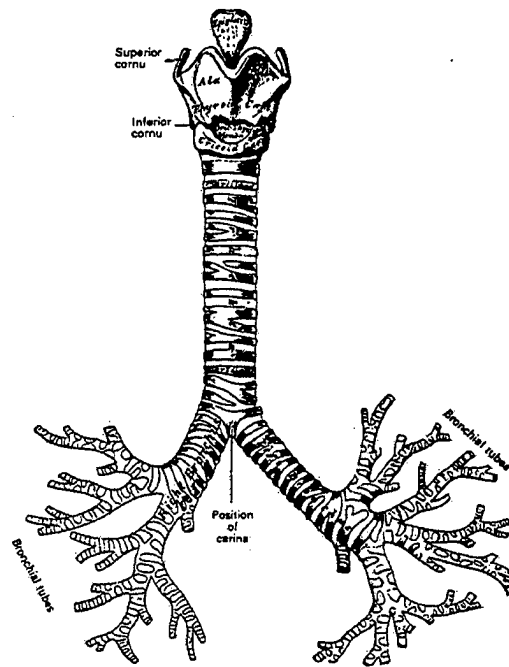


Figure 11. Trachea and Bronchi. From Ref. [2].

The heart is divided into two halves, right and left, by a wall called the septum. Each half is divided into an upper and lower part by a horizontal partition. The upper halves are the auricles (atria) and the lower halves are the ventricles. Thus the heart consists of four chambers, right auricle, right ventricle, left auricle, and left ventricle for the left half. The left and right halves of the heart are completely separate, but the auricle and the ventricle of the same half of the heart opens into each other. The heart is enclosed by a concentric membrane sac called the pericardium. The pericardium consists of two layers, an external fibrous and an internal serous. The fibrous layer is a strong dense membrane that surrounds the great vessels that leave and enter the heart and is attached to the diaphragm. The inner (visceral) surface of the serous layer is adherent to

the heart and encloses the heart. The outer (parietal) surface of the serous layer is reflected on the inner surface of the fibrous layer. The heart is depicted in Figure 12.

[Refs. 1 & 2]

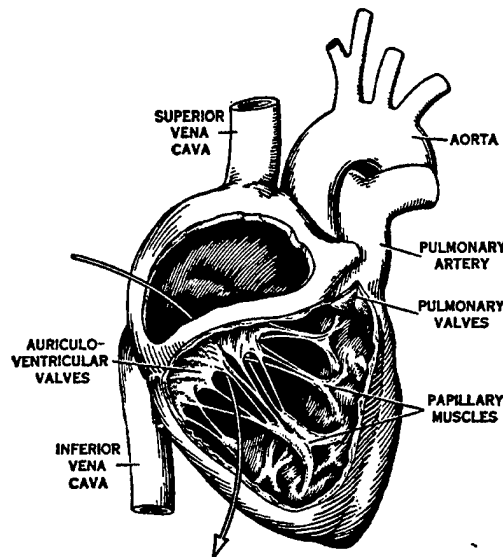


Figure 12. The Right Side of the Heart with the Wall of the Atrium and Ventricle Cut Away. From Ref. [1].

The right half of the heart contains venous blood and the left half contains pure arterial blood. The left ventricle pumps pure blood into the aorta, which is distributed throughout the body, except for the lungs. The pure blood as it passes through the body, releases materials to nourish the tissues thorough the capillaries. The pure blood receives the impurities and becomes venous. The blood returns from the capillaries via the superior and inferior vena cava to the right auricle. From the right auricle, the blood is passed into the right ventricle. The right ventricle pumps the blood into the lungs through the pulmonary arteries. In the capillaries of the lungs, the blood becomes pure and is returned to the left auricle via the pulmonary vein. The blood is passed into the left ventricle and the process starts again. [Refs. 1 & 2]

### **C. LITERATURE SURVEY**

The major areas of study on the human thorax have been creating and validating a finite element model of the human thorax and the biodynamical response of human thorax from a blunt impact during an automobile collision. There have been few studies on the biodynamical response of the human thorax to a projectile impact.

The modeling of the human thorax began with determining the thorax's biomechanical response to static loads. Roberts and Chen [Ref. 3] developed an elastostatic finite element model of the human thorax using gross geometric data and approximate cross-sectional properties. The sternum of the model was placed under various static loads and the displacement of the sternum was measured. The model was validated by obtaining reasonable data for the sternum displacement. Their model is used for the basis for the development of the model used in this study. Andriacchi, Schultz, and Belytschko and Galante [Ref. 4] developed a model of the human thorax to study the interactions between the human spine and rib cage. They used the model of the thorax by Roberts and Chen [Ref. 3] as a base and then refined the model. From their work, they determined the influence the rib cage plays on the bending response of the spine, the lateral stability of the spine, and the mechanisms of scoliotic deformities. Their model was validated by comparing rib cage deflection under a static load to experimental results.

Further development of the finite element model of the human thorax began with modeling of the organs in the human thorax and determining the biomechanical response to static loads. Sundaram and Feng [Ref. 5] modeled a three dimensional thorax using beam elements for the rib cage, shell elements for the sternum, membrane elements for

the muscles and solid elements for the internal organs. The model assumed linear elastic behavior for all materials and that the thorax is symmetrical. There was no detail modeling of the internal organs and the boundaries between different organs and tissues were assumed to be continuous. The model was loaded statically and verified against cadaver experiments.

The need to determine the dynamic response of the human thorax to blunt impacts, such as in automobile accidents, led to additional developments of the finite element model of the thorax. Chen [Ref. 6] developed a finite element model of the human thorax using beam elements to study its impact response under dynamic loading. The model contains the 10 rib pairs, vertebral column, and sternum. Chen assumed the internal organs would have no effect on the model's response and lumped the internal organs at the thoracic wall. The model also assumed linear elastic behavior for all materials. The model was validated by comparing the force-deflection and deflection time curves of the model to cadaver experiments. Plank and Epplinger [Ref. 7] developed a model of the human thorax to study its dynamic response to frontal impact during an automobile accident. Their model assumed linear elastic material properties except for the internal organs that were modeled as a viscoelastic material. Their model does not take into account the nonlinear interactions of the internal organs. The finite element model was validated by comparing the model's force deflection curves to cadaver experiments. Wang [Ref. 8] developed a model of the human thorax with detailed organ description to determine its dynamic response to a side impact during an automobile accident. The model took into account the nonlinear interfacing among organs using frictionless sliding contact elements. Wang assumed linear elastic behavior

for all materials except for the heart and lungs. The heart and lungs were treated as viscoelastic materials. Comparing the force-time and force-deflection curves of the model to cadaver experiments validated the model.

Research has been made on the material properties of the thorax and its viscera in addition to developing three-dimensional models of the human thorax. Yogananda and Pinter [Ref. 9] determined the material properties of the seventh and eighth rib pairs for 30 cadavers. Yogananda and Pinter determined the cross-sectional area, moment of inertia, failure load, deflection, and Young's Modulus using three-point bending techniques on isolated ribs. Yamada [Ref. 10] determined the material properties for tissues, organs, and bones located in the human body.

The need for determining the dynamic response of the human thorax with body armor to projectile impacts led to the models developed by Hughes [Ref. 11] and Jolly [Ref. 12]. Hughes developed a three-dimensional model of the thorax using data from Andriacchi, et al [Ref. 4] and Yogananda, et al [Ref 9]. The computed response of the finite element model to an applied static load was studied to validate Hughes's model. In addition, Hughes performed a limited study on the dynamic response of the thorax to a projectile impact with his model. The data from the thoracic model developed by Hughes correlated with the data from the cadaver experiments. However the sternum response showed large oscillations compared to the cadaver results. The large oscillations are believed to be caused by the lack of damping in his model. Jolly developed his model of the thorax by using Hughes model as the basis for his model. Jolly incorporated the soft tissues and muscles of the thorax to provide the damping in his model to minimize the oscillations of the thorax to projectile impact. Jolly's model was validated by comparing



the model's results to experimental data obtain from cadavers undergoing projectile impact. Jolly's and Hughes's models did not include the major internal organs in the thorax such as the heart and lungs.

The only existing cadaver study of the thorax's biodynamical response to bullet impact with body armor was performed by DeMaio, et al the Armed Forces Institute of Pathology [Ref. 13]. Cadavers were suspended to a wood board wearing body armor consisting of Kevlar or Kevlar with one of two variations of a Boron Carbide plate. The cadavers wearing body armor consisting of Kevlar were struck with a NATO 9 mm round. The cadavers wearing body armor consisting of Kevlar plus one of two variations of a boron carbide plate were struck with a NATO **7.62** mm M80 ball round. The firing distances for all cases were 50 feet. The recorded parameters are the accelerations of the trachea, aorta, spine, sternum, and ligament arteriosum, right and left ventricular pressures and the displacement and velocity of the sternum and spine. Autopsies were performed on the cadavers to determine the extent of their injuries.

**THIS** PAGE INTENTIONALLY LEFT BLANK

### III. FINITE ELEMENT MODEL

#### A. HUMAN THORACIC MODEL

The skeletal portion of the human thorax is created from the geometric data of the thorax from work by Andriacchi, et al [Ref. 4] and Roberts and Chen [Ref. 3] which was later adopted by Hughes [Ref. 11] and Jolly [Ref. 12]. The viscera (heart lungs, great vessels, bronchi and trachea) of the thorax are developed from cross sectional views of the human anatomy by Bo, et al [Ref. 14]. The cross sectional views of the thorax are used to interpolate the positioning of the viscera in the thorax of cadavers to the cross sectional views of the skeleton model of the thorax. Figure 13 depicts the model created for this study.

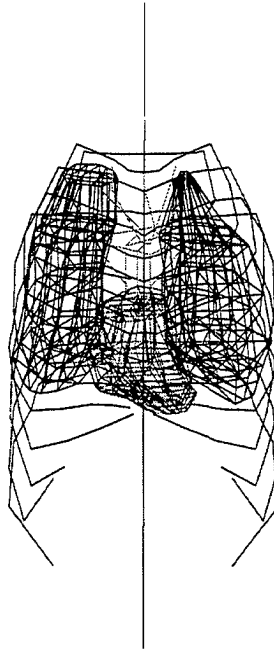


Figure 13. Anterior View of the Human Thorax

The finite element program that is used for analysis is DYNA3D available from Lawrence Livermore National Laboratories. The particular version used was DYNA3D version N-12.

### **1. Modeling of the Thoracic Skeleton**

Ribs pairs 1 – 10 are modeled as beam elements. The floating rib pairs, rib pairs 11 – 12, are not modeled. Each rib consists of thirteen beam elements. The beam elements for each rib are given specified cross sectional properties to maintain the correct size, shape, and angle of the head and tuberosity of the rib. The ribs are assumed to be composed of only compact bones and are modeled as a linear elastic material. [Ref. 12]

The spine is modeled with a series of beam elements. Each vertebra is modeled with two beam elements. The intervertebral disc between the vertebrae is modeled with one beam element. Two beam elements are used to model the facet joint with the end of each beam connected to the midpoint of an adjacent vertebra. The spine is shown in Figure 14. [Ref. 12]

The sternum is modeled with thin shell elements. The thin shell elements have a thickness of 0.25 inches. The sternum is depicted in Figure 15. [Ref. 12]

The muscle is modeled with 24 solid elements as shown in Figure 16. The thickness of the elements is varied to accurately model the curvature of the muscles along the anterior side of the thorax. The thickness of the solid elements ranges from 0.25 inches along the central, anterior edge of the sternum to 2.35 inches at the most distal position of rib #4. In addition, springs and dampers are used between the muscles and ribs to portray the correct viscous nature of muscle and transfer of force to the ribs. [Ref. 12]

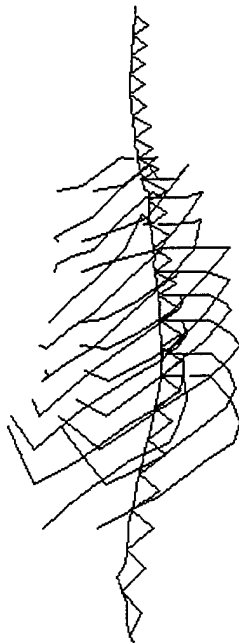


Figure 14. Medial View of the Ribs and Spine. From Ref. [12].

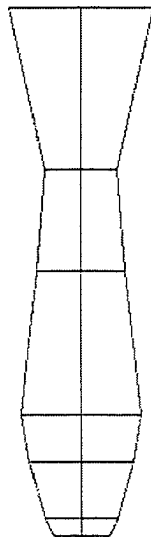


Figure 15. Anterior View of the Sternum. From Ref. [12].

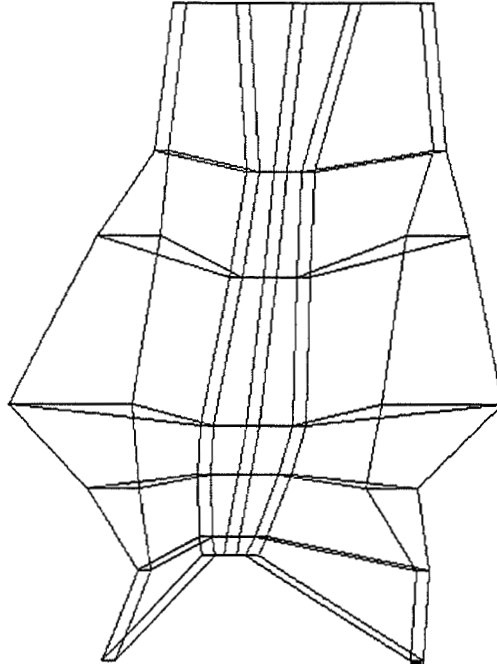


Figure 16. Muscle on the Thoracic Skeleton. From Ref. [12]

Beam elements are used to model the cartilage connections of the thorax as depicted by the darker lines in Figure 17. The sternochondral joint is modeled with one beam element. The articular cartilage between the rib and vertebrae is modeled with two beam elements. To create the subcoastal angle, vertical cartilaginous connections at the inferior edge of the sternum are modeled as beam elements. [Ref. 12]

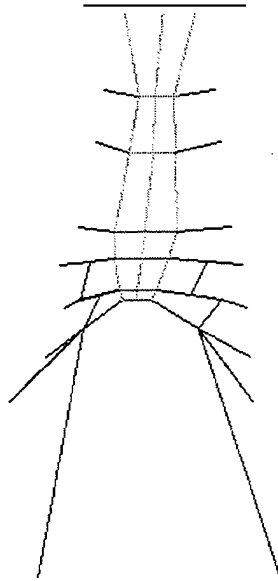


Figure 17. Articular Cartilage Connecting Sternum and Ribs. From Ref. [12].

## 2. Modeling of the Viscera in the Human Thorax

The right and left lungs are modeled as solid elements as depicted in Figure 18. The fissures between the lungs are not modeled and the each lung is treated **as** a whole solid object. The two layers of pleura that enclose each lung are modeled with one layer of thin shell elements directly attached to the lungs. The bronchus from each lung and the trachea are modeled with circular hollow beam elements. The trachea is attached to the first rib pair with a single beam that has properties similar to the first rib pair. Spring and damper elements are used between the lungs and the ribs to transfer force from the bullet impact to the lungs.

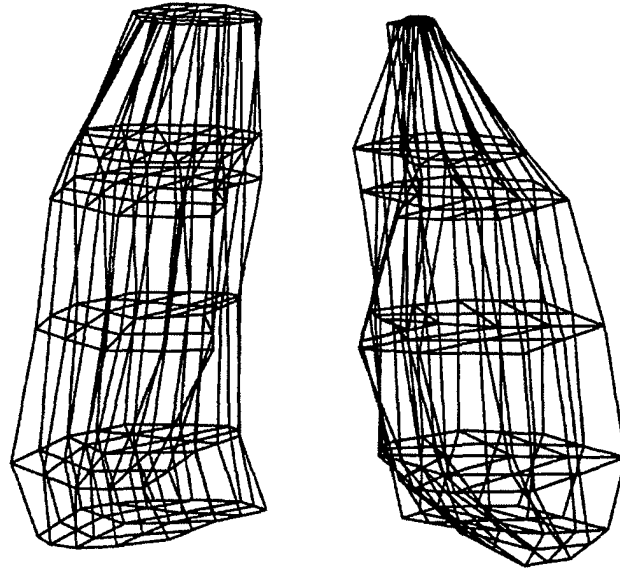


Figure 18. Anterior View of the Lungs

The heart is modeled with solid elements as depicted in Figure 19. The model of the heart does not distinguish between the left and right ventricles and the left and right auricles due to the experimental measurements being very similar for the right and left ventricles. The blood within the heart is modeled with a Grunesian equation of state with cubic shock velocity to determine the pressure within the heart. The Grunesian equation of state is listed below:

$$P = \frac{\rho_o C^2 \mu \left[ 1 + \left( 1 - \gamma_o / 2 \right) \mu - \left( a / 2 \right) \mu^2 \right]}{\left[ 1 - (S_1 - 1) \mu - S_2 \left( \mu^2 / (\mu + 1) \right) S_3 \left( \mu^3 / (\mu + 1) \right) \right]^2} + (\gamma_o + a \mu) E$$

C -intercept of the  $\mu_s - \mu_p$  curves

S 1, S2, S3 - coefficients of the slope of the  $\mu_s - \mu_p$  curve

$\gamma_o$  - Grunesian gamma

$\mu$  - absolute viscosity.



The values assigned for use in the Grunesian equation are located in Table 1. There is no distinction made between the pure and venous blood. The two layers of the pericardium are modeled as one layer of shell elements directly attached to the heart. Spring and damper elements are used between the heart and lungs to model their interaction. Also, spring and damper elements are used between the heart and sternum to transfer the force from the bullet impact to the heart.

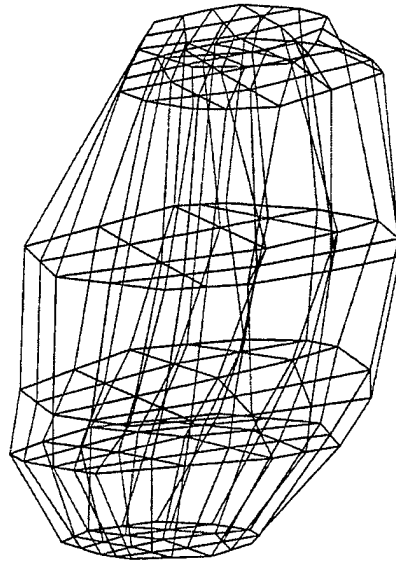


Figure 19. Anterior View of the Heart

The vessels in the thorax that are modeled are the common carotids, the brachiocephalic aorta, the aorta, pulmonary arteries and veins, internal jugular veins, brachial veins, and superior vena cava. These vessels are modeled as circular hollow beam elements. For the vessels that extended up to the first rib pair, each vessel is attached to the first rib pair with a single beam having properties similar to the first rib pair.

## B. ARMOR

The biodynamical response of the thoracic model to a projectile impact is analyzed using two different types of body armor on the thoracic model. The first type of body armor used consisted of a Boron Carbide plate placed over a sheet of Kevlar. The second type consisted of the sheet of Kevlar only. The body armor system with the boron carbide plate and Kevlar is modeled with thick shell elements. The Boron Carbide plate consisted of 126 thick shell elements with a thickness of 0.5 inches. The Boron Carbide plate is directly attached to the Kevlar sheet. The Kevlar sheet is also modeled with 126 thick shell elements with a thickness of 0.25 inches. The Kevlar sheet is modeled on the thoracic model so that it is projected directly across the most anterior points of the muscle tissue as shown in Figure 20. Modeling the Kevlar sheet on the thoracic model in this manner, creates a gap between the muscle and the Kevlar sheet above the sternum, which represented the actual placement of the body armor when worn. The body armor system consisting of the Kevlar sheet only is modeled just like the Kevlar and boron carbide plate armor system with the boron carbide plate removed. [Ref. 12]

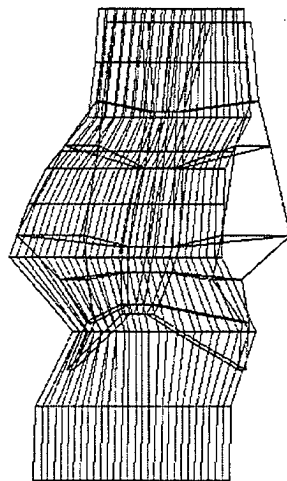


Figure 20. Kevlar Vest Overlaying the Thoracic Muscle. From Ref. [12].

### **C. INTERFACE ELEMENTS**

Contact elements are used between the vest and the muscle interface to prevent rigid body motion of the body armor after bullet impact. The contact elements allow movement of the vest in one direction to impart a force upon the chest on bullet impact while movement of the vest in the other direction creates a separation between the chest and armor without transfer of force. [Ref. 12]

### **D. PROJECTILE**

The projectile is modeled as a single element attached directly to the most anterior body armor component on the Kevlar or Boron Carbide plate depending what type of body armor is being used during the test run as shown in Figure 21. The projectile is modeled to provide impact but no penetration. The solid element that represents the projectile is given the material properties and dimensions of either a NATO 7.62 mm Ball **M80** round or a NATO 9mm full metal jacket round. The most anterior four nodes of the projectile are given an initial velocity to model the projectile motion. This allows the momentum of the bullet to be transferred to the body armor. The initial velocity of the NATO 7.62 mm round and the NATO 9mm round are 966 m/s and 500 m/s respectively. These initial velocities were determined experimentally at test firings by DeMaio, et al [Ref. 13] at the Aberdeen Proving Grounds in Maryland. [Ref. 12]

### **E. BOUNDARY CONDITIONS**

The boundary conditions that are used for the thoracic model are based on the experimental setup used during the cadaver studies at Armed Forces Institute of Pathology. The cadavers are placed flat on a wooden board and secured to the board using wires. The most posterior nodes of each rib pair are constrained in translation to represent the experimental setup. [Ref. 12]

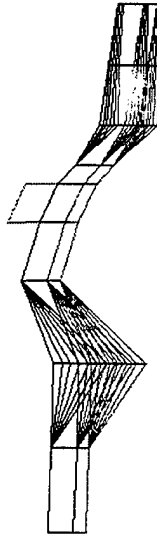


Figure 21. Medial View of the Projectile Attached to Kevlar and Boron Carbide Plate Body Armor System. From Ref. [12].

## F. MATERIAL PROPERTIES

The material properties of the human body are difficult to model. The material properties of soft tissues vary in relaxation and contraction. There is also a wide variation of the material properties of the human body due to age, sex, and size of an individual. The material properties of the human body that are published are mainly based on static testing vice dynamic testing **and** performed on cadavers. The material properties of cadaver tissues differ from living tissues.

The response of a soft tissue to an axial force is shown in the force deflection curve **as** shown in Figure 22. The force deflection curve consists of three regions. The first region, O to A, is an initial exponential region. This region is the physiological range where the tissue normally functions. The second region, A to B, is linear and the third region from B to C is nonlinear and rupture occurs. The second and third regions represent the reserve strength of the tissues. [Ref. 15]

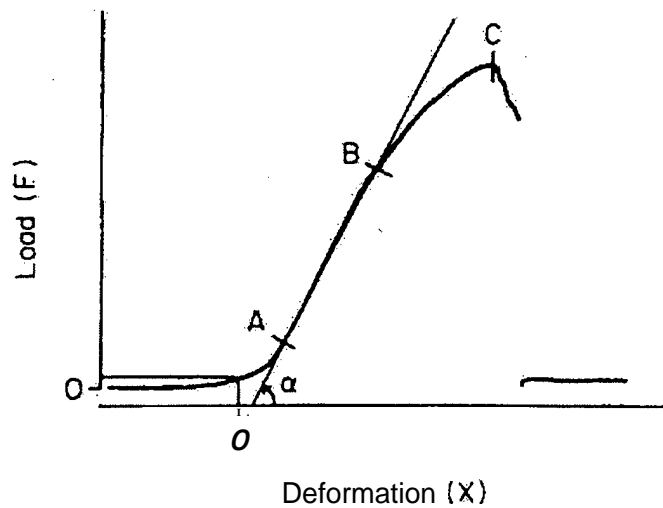


Figure 22. Load-Elongation Curve for a Rabbit Lamb Tendon Bought to Failure with Constant Rate of Elongation. From Ref. [15].

For this model, the material properties of all soft tissues, except the muscle of the thorax, are based on the linear portion of the force deflection curve for soft tissues. All soft tissues are assumed to be linear elastic materials with the exception of the muscle. The muscle of the thorax is modeled as a viscoelastic material based on the study completed by Jolly [Ref. 12]. Jolly modeled the muscle as a viscoelastic material to provide the necessary damping for the model of the thorax. The material properties of the soft tissues with the exception of the muscle are adopted from the work done by Wang. [Ref. 8]

The components of the thoracic skeleton are modeled as a linear elastic material. The material properties of the ribs are based on the work done by Yogananda and Pinter [Ref. 9]. They determine the material properties for the seventh and eighth ribs of multiple subjects. Their “average” values are used to determine the material properties for each

element in each rib pair. The ribs are assumed to be composed of compact bone. The work done by Sundaram, et al [Ref 5] and Andriacchi, et al [Ref 4] is used to derive the material properties of the vertebrae and vertebral disc. The compact bone properties of rib 4 are used to derive the material properties for the sternum. [Ref. 12]

The material properties of the body armor are subject to some guesswork due to the proprietary nature of these materials. Realistic values are used for the body armor. The body armor is modeled as a linear elastic material. The material properties of the Kevlar are assumed to be a density of  $1440 \text{ kg/m}^3$ , a Young's Modulus of 1 GPa and a Poisson's ratio of 0.2. The boron carbide plate's material properties are assumed to be a density of  $2500 \text{ kg/m}^3$ , a Young's Modulus of 448 GPa, and a Poisson's ratio of 0.2. [Ref. 12]

The material properties of the human thorax are listed in Table 1. There is some variation in the material properties for the two test cases due to the difference in age of the cadavers used. In the first test case, determining the biodynamical response of the thorax with body armor consisting a Kevlar sheet and Boron Carbide plate being struck by a NATO 7.62 mm ball M80 round, specimen 801, the age of the cadaver is 41. In the second test case, determining the biodynamical response of the thorax with body armor consisting a Kevlar sheet only being struck by a 9mm Full Metal Jacket Round, specimen 678, the age of the cadaver is 92.

	Specimen 801	Specimen 678
Thorax Component	Material Property	Material Property
Ribs	E = 2.83 GPa $\rho = 1000 \text{ kg/m}^3 \quad \nu = 0.2$	E = 2.83 GPa $\rho = 1000 \text{ kg/m}^3 \quad \nu = 0.2$
Vertebra and Facet Joints	E = 12.13 GPa $\rho = 1000 \text{ kg/m}^3 \quad \nu = 0.2$	E = 12.13 GPa $\rho = 1000 \text{ kg/m}^3 \quad \nu = 0.2$
Vertebral Discs	E = 1.5 GPa $\rho = 1000 \text{ kg/m}^3 \quad \nu = 0.2$	E = 1.5 GPa $\rho = 1000 \text{ kg/m}^3 \quad \nu = 0.2$
Sternum	E = 12.13 GPa $\rho = 1000 \text{ kg/m}^3 \quad \nu = 0.2$	E = 12.13 GPa $\rho = 1000 \text{ kg/m}^3 \quad \nu = 0.2$
Sternochondral Junction Cartilage	E = 64.7 MPa $\rho = 1000 \text{ kg/m}^3 \quad \nu = 0.2$	E = 64.7 MPa $\rho = 1000 \text{ kg/m}^3 \quad \nu = 0.2$
Chondracostal Cartilage	E = 5 MPa $\rho = 1000 \text{ kg/m}^3 \quad \nu = 0.2$	E = 5 MPa $\rho = 1000 \text{ kg/m}^3 \quad \nu = 0.2$
Pleura or Pericardium	E = 0.4 GPa $\rho = 2000 \text{ kg/m}^3 \quad \nu = 0.4$	E = 0.4 GPa $\rho = 2000 \text{ kg/m}^3 \quad \nu = 0.4$
	E = 0.004 GPa $\rho = 2000 \text{ kg/m}^3 \quad \nu = 0.4$	E = 0.0004 GPa $\rho = 2000 \text{ kg/m}^3 \quad \nu = 0.4$
Pulmonary Arteries	E = 0.004 GPa $\rho = 2000 \text{ kg/m}^3 \quad \nu = 0.4$	E = 0.0004 GPa $\rho = 2000 \text{ kg/m}^3 \quad \nu = 0.4$
Pulmonary Veins	E = 0.02 GPa $\rho = 2000 \text{ kg/m}^3 \quad \nu = 0.4$	E = 0.002 GPa $\rho = 2000 \text{ kg/m}^3 \quad \nu = 0.4$
Superior Vena Cava	E = 0.02 GPa $\rho = 2000 \text{ kg/m}^3 \quad \nu = 0.4$	E = 0.002 GPa $\rho = 2000 \text{ kg/m}^3 \quad \nu = 0.4$
Heart	E = 0.167 MPa $\rho = 1000 \text{ kg/m}^3 \quad \nu = 0.4$	E = 0.167 MPa $\rho = 1000 \text{ kg/m}^3 \quad \nu = 0.4$

Table 1. Material Properties of the Human Thorax

Lungs	$E = 0.002 \text{ MPa}$ $\rho = 600 \text{ kg/m}^3 \quad \nu = 0.4.$	$E = 0.002 \text{ MPa}$ $\rho = 600 \text{ kg/m}^3 \quad \nu = 0.4$
Common Carotids	$E = 4 \text{ MPa}$ $\rho = 2000 \text{ kg/m}^3 \quad \nu = 0.4$	$E = 0.4 \text{ MPa}$ $\rho = 2000 \text{ kg/m}^3 \quad \nu = 0.4$
Internal Jugular Veins	$E = 4 \text{ MPa}$ $\rho = 2000 \text{ kg/m}^3 \quad \nu = 0.4$	$E = 0.4 \text{ MPa}$ $\rho = 2000 \text{ kg/m}^3 \quad \nu = 0.4$
Brachial Veins	$E = 4 \text{ MPa}$ $\rho = 2000 \text{ kg/m}^3 \quad \nu = 0.4$	$E = 0.4 \text{ MPa}$ $\rho = 2000 \text{ kg/m}^3 \quad \nu = 0.4$
Trachea	$E = 0.01 \text{ GPa}$ $\rho = 2000 \text{ kg/m}^3 \quad \nu = 0.4$	$E = 0.001 \text{ GPa}$ $\rho = 2000 \text{ kg/m}^3 \quad \nu = 0.4$
Brachiocephalic Aorta	$E = 4 \text{ MPa}$ $\rho = 2000 \text{ kg/m}^3 \quad \nu = 0.4$	$E = 0.4 \text{ MPa}$ $\rho = 2000 \text{ kg/m}^3 \quad \nu = 0.4$
Muscle	$G = 0.5 \text{ MPa} \quad G_o = 0.1 \text{ MPa}$ $G_\infty = 0.01 \text{ MPa} \quad \beta = 1000$	$G = 0.5 \text{ MPa} \quad G_o = 0.1 \text{ MPa}$ $G_\infty = 0.01 \text{ MPa} \quad \beta = 1000$
Blood	$C = .148\text{E}4 \quad S1 = 1.75$ $S2 = 0 \quad S3 = 0 \quad \gamma_o = 0.28$ $\mu = 0.01 \text{ Ns/m}^2$	$C = .148\text{E}4 \quad S1 = 1.75$ $S2 = 0 \quad S3 = 0 \quad \gamma_o = 0.28$ $\mu = 0.01 \text{ Ns/m}^2$

Table 1. Material Properties of Human Thorax (cont.)



### III. RESULTS AND DISCUSSION

After the development of the finite element model of the human thorax, an analysis of the model is conducted to determine if the model adequately predicts the biodynamical response of the thorax to projectile impact. The first analysis is the response of the model with a body armor consisting of Kevlar sheet and a Boron Carbide plate struck by a NATO 7.62 mm M80 ball. The second analysis is the response of the model with body armor consisting of a Kevlar sheet struck by a NATO 9mm round. Each analysis ran for a duration of two milliseconds. For both analyses, the model is deemed valid from the comparison of the model's results to experimental data, provided by DeMaio, et al [Ref. 13], of cadavers undergoing projectile impact testing. The parameters that are compared are the acceleration in the anterior to posterior direction for the T7 vertebra, the center of sternum, the pulmonary artery at the ligamentum arteriosum, and the trachea at the carina and ventricle pressure. Also the velocity and displacement of the sternum and T7 vertebra in the anterior to posterior direction are used for comparison. The data obtained from the model's analysis is subsequently smoothed using a simple twelve-point averaging method to remove aberrant oscillations. The experimental data is provided as text files with time and parameter recorded. The experimental data did not require any processing. The experimental results for the velocity and displacement of the vertebrae and sternum are obtained from numerical integration of their accelerations. Thus, the accelerations of the sternum and T7 vertebra are used as the primary comparison between the model's results and experimental data. The standard used for comparisons is the times and magnitudes of the peaks and overall

trend of the parameter. Once the model is deemed valid, a parametric study is conducted to determine the essential components of the model.

## **A. VIABILITY STUDY**

### **1. Human Thorax Model with Kevlar and Boron Carbide Plate Body Armor System Struck by NATO 7.62mm Ball M80 Round**

The biodynamical response of the human thorax model with a Kevlar and Boron Carbide plate body armor being struck by a NATO 7.62 mm M80 ball round with an impact velocity of 966m/s is examined. The parameters that are used for comparison between the model's results and the experimental results are the sternum, spinal, trachea, and pulmonary accelerations, velocity and displacement of the sternum and spine in the anterior to posterior direction, and ventricle pressure.

Comparing the sternum acceleration from the finite element model of the human thorax to the experimental results, the correlation is excellent as shown in Figure 23. The magnitude of the initial peak acceleration, the time of the peak, and the trough for the model is similar to the experimental results. The discrepancy between the model and experimental results of the sternum acceleration up to **0.2** msec is possibly due to the movement of the wire of the accelerometer upon impact. DeMaio et al [Ref 13] reports that wire movement of the accelerometers caused erratic readings. Also approximately at 1msec, there is another discrepancy between the model's and experimental results for the sternum acceleration. The magnitude of the sternum acceleration for the experimental results is much greater compared to the model's result. The possible cause for this discrepancy is due to massive sternal fractures. Upon completion of projectile testing, a

postmortem examination of specimen 801 showed massive sternal fractures. The sternal fracture will reduce the stiffness of the sternum thus allowing for greater accelerations. The finite element model did not take into account the failure of the bone due to fracture. Otherwise there is excellent correlation between results for sternum acceleration.

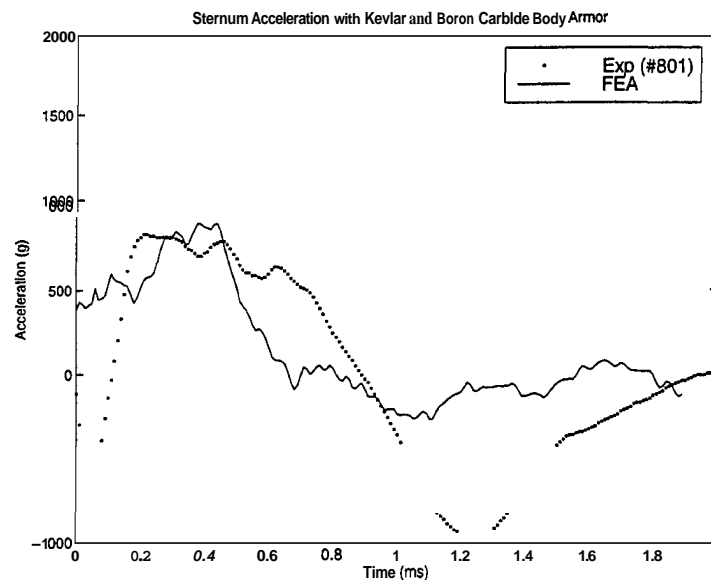


Figure 23. Sternum Acceleration (Kevlar and Boron Carbide). After Ref. [13].

The model's results for sternum velocity does not correlate as well compared to the experimental data as shown in Figure 24. The initial dip in velocity upon impact is due to the acceleration going the opposite direction to the impact direction. Demaio, et al [Ref. 13] recorded acceleration and used numerical integration to obtain velocity and displacement results. Any discrepancies in the sternum acceleration results will propagate to the velocity and displacement results. Thus, the acceleration results are considered more fundamental to validation of the model. At approximately **1.2** msec, the magnitudes of the velocities start to differ. The reason for the discrepancy is again due to the numerical integration techniques used to obtain velocity results. After

approximately 1 msec, the magnitude of the experimental sternum acceleration in the opposite direction to impact direction is greater compared to the model's results. This difference in magnitudes leads to the discrepancy between the velocities after 1 msec.

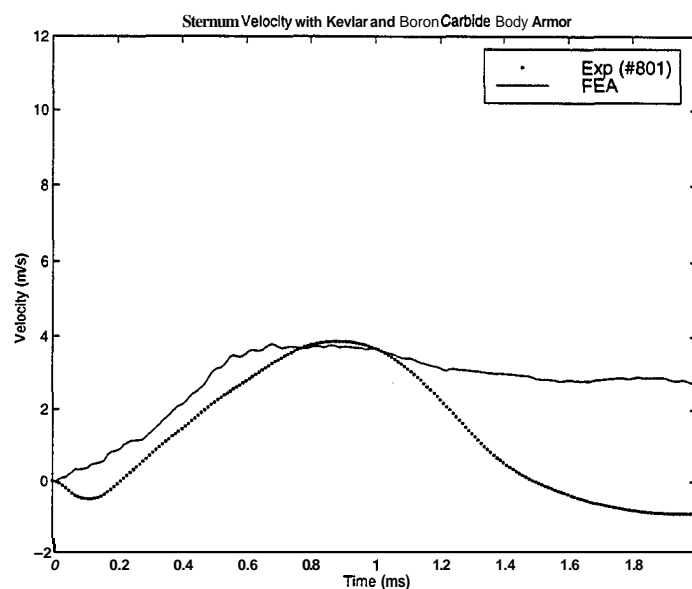


Figure 24. Sternum Velocity (Kevlar and Boron Carbide). After Ref. [13].

The model's results for sternum displacement do not correlate very well compared to the experimental results. The discrepancies between the displacements are due to the differences in the experimental and model's results for acceleration. Demaio, et al [Ref. 13] estimated about 30 millimeters of sternum displacement at approximately 30 msec, through experimental observation. The displacement is obtained at the end of the data-recording period. The experimental results do not show this in Figure 25. If the model's results were extrapolated to 30 msec, the displacement would be approximately 25 to 30 mm. Thus the model adequately predicts the displacement of the sternum.

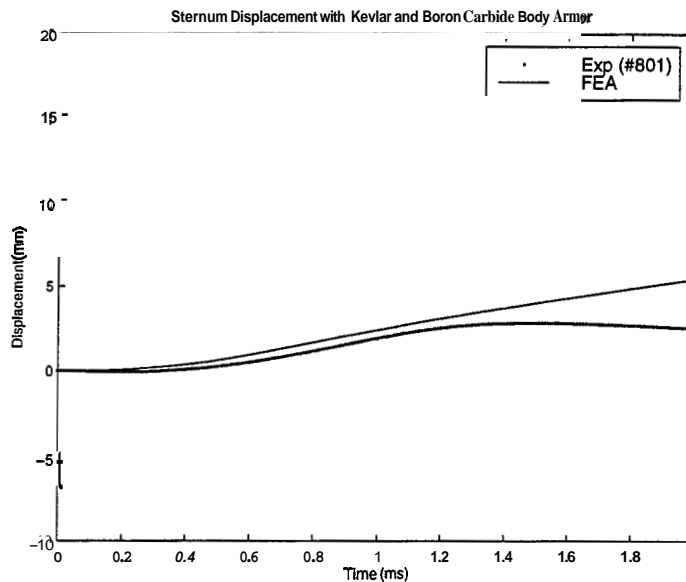


Figure 25. Sternum Displacements (Kevlar and Boron Carbide). After Ref. [13].

The spinal acceleration results for the model and the experiment data correlated well as illustrated in Figure 26. The spinal acceleration magnitude for the experimental and model's results is approximately the same up to 1msec. After 1 msec, there is a discrepancy in the spinal acceleration magnitude. The discrepancy is possibly due to the massive sternal fractures occurring at that time. When the massive sternal fractures occur, the sternum will no longer support the ribs. The ribs, not being rigidly supported, will bend at a greater rate thus increasing the spinal acceleration. The spinal velocity and the spinal displacement are shown in Figures 26 and 27, which show the same correspondence as the acceleration due to the numerical integration of acceleration to obtain the experimental results for velocity and displacement.

Comparing the results of this thorax model to Jolly's model [Ref. 12] the acceleration, velocity, and displacement of the sternum and spine correlated very well.

The magnitude of the acceleration, velocity, and displacement of the sternum and spine were slightly lower compared to Jolly's model. Modeling the organs increased the overall stiffness of the model thus lowering the magnitude of the acceleration, velocity, and displacement of the sternum and spine.

The model's pulmonary acceleration results correlate with the experimental results as shown in Figure 29. The magnitude and trend of the model's and experimental results are very similar. The experimental data shows oscillating motion, which is due to the local alternating motion of the pulmonary artery. The model's pulmonary acceleration results are concerned with the global acceleration of the pulmonary artery. As such, there is no localized alternating motion in the model's results as seen in the experimental results.

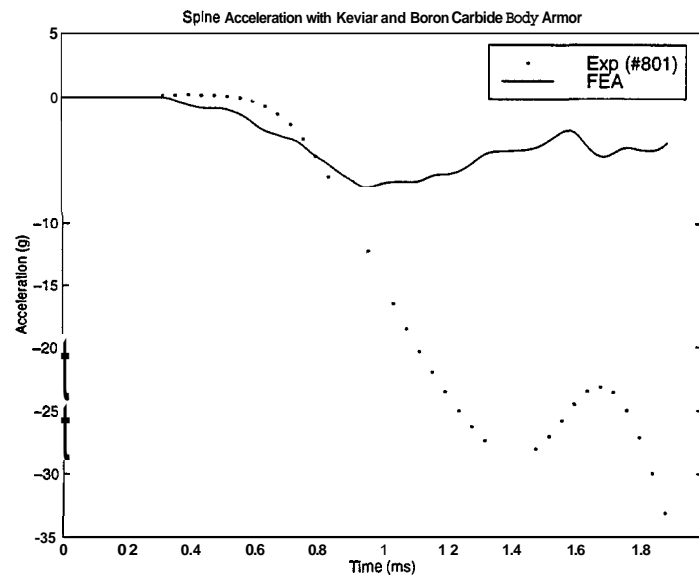


Figure 26. Spinal Acceleration (Kevlar and Boron Carbide). After Ref. [13].

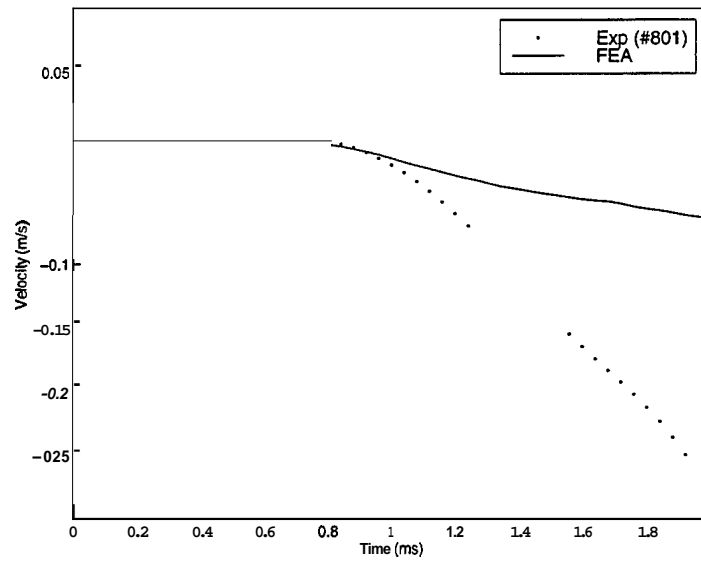


Figure 27 Spinal Velocity (Kevlar and Boron Carbide). After Ref. [13].

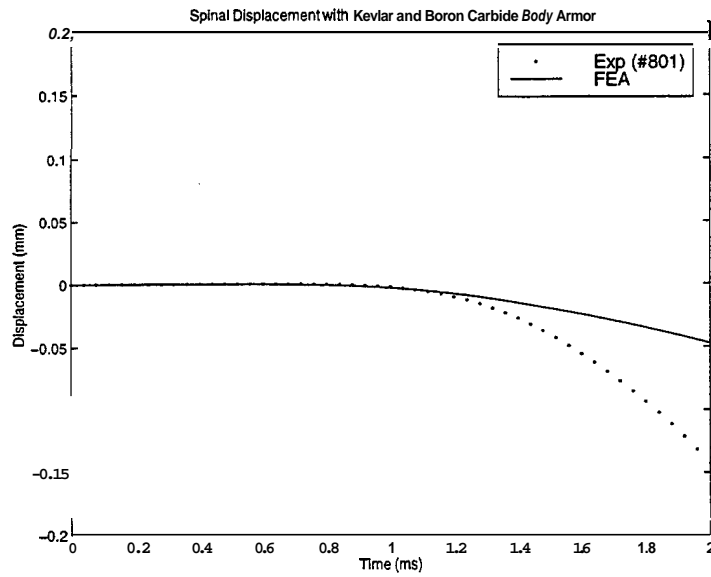


Figure 28. Spinal Displacement (Kevlar and Boron Carbide). After Ref. [13].

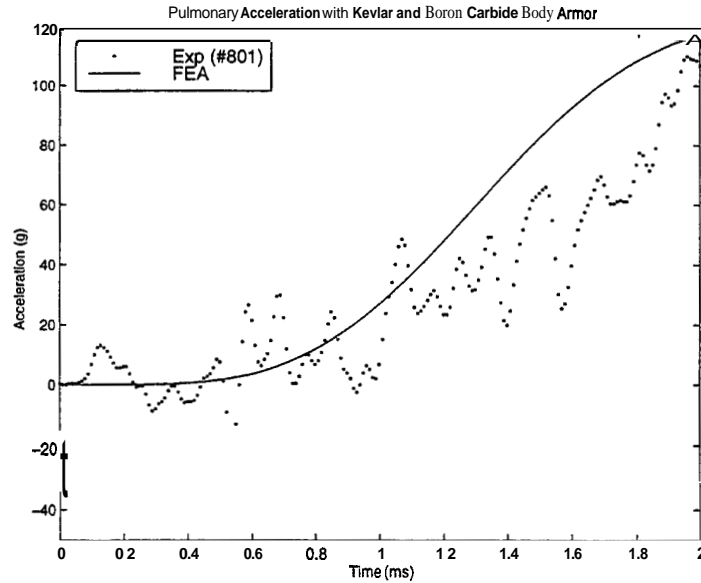


Figure 29. Pulmonary Artery Acceleration (Kevlar and Boron Carbide). After Ref. [13].

The correlation between the model's results and the experimental results for the trachea acceleration is fair as depicted in Figure 30. The magnitude of the trachea peak acceleration for the model and the experiment results is similar. The overall trend of the acceleration results for the model and the experimental results also correlate. However there is a discrepancy between the time when the peak acceleration occurs for the experimental and model results. A reason for the discrepancy is how the trachea is modeled. For this model, the trachea is attached to the first rib with a beam support that has material properties of the first rib. The trachea actually extends beyond the first rib pair up to the neck and head. The head and neck would have to be modeled to reflect the correct time of peak acceleration.



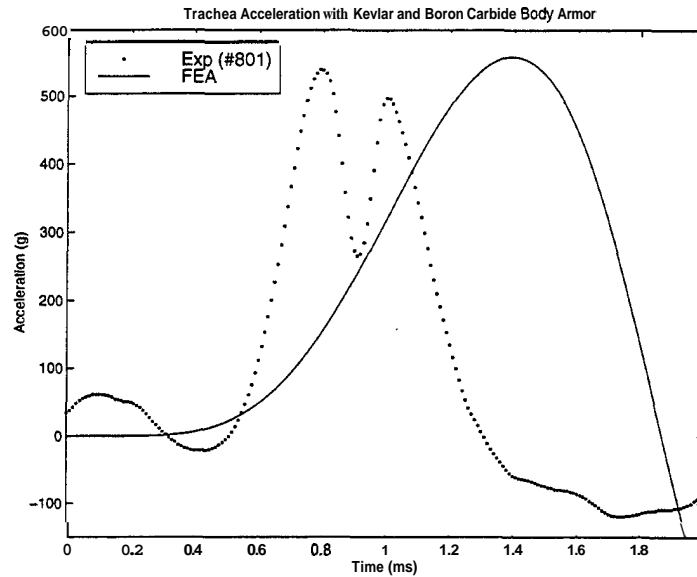


Figure 30. Trachea Acceleration (Kevlar and Boron Carbide). After Ref. [13].

The ventricle pressure of the model compared to the experimental results correlated in terms of magnitude and general trend as shown in Figures 31 and 32. The oscillations in the ventricle pressure are due to the local movement of the heart upon bullet impact. Also the location of where the ventricle pressure is monitored has an effect. Comparing Figures 31 and 32, there is a difference in the model's ventricle pressure due to the ventricle pressure being monitored at different locations within the ventricle. Thus, where the ventricle pressure is measured will have a big effect on the model or experimental results.

Based on the comparison of the parameters described above, the model is deemed valid. The model's results show the same correlation as the experimental results. In addition, the magnitude of the parameters for the model and experimental results is similar.

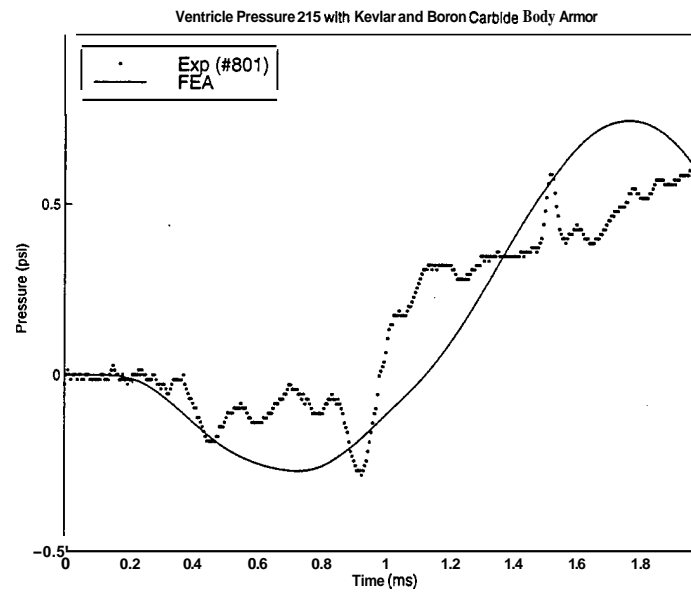


Figure 31. Ventricle Pressure Element 215 (Kevlar and Boron Carbide). After Ref. [13].

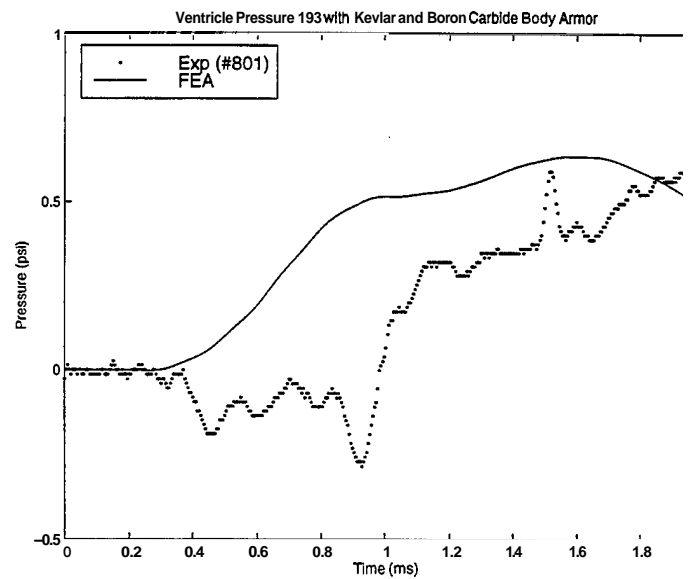


Figure 32. Ventricle Pressure Element **193** (Kevlar and Boron Carbide). After Ref. [13].

## **2 Human Thorax Model with Kevlar Body Armor Struck by a NATO 9mm Full Metal Jacket Round**

The biodynamical response of the thorax model with Kevlar body armor being struck by a NATO 9 mm full metal jacket round with an impact velocity of 500m/s is examined. The same parameters except trachea acceleration, as in the previous test case are used for comparison between the model and experimental results

The correlation between the model's results and the experimental results is fairly high for the sternum acceleration as shown in Figure 33. The time for the first and second peaks of acceleration occurred at the same time. The magnitude of the first peak for the model is slightly higher and the magnitude of the second peak is slightly lower. The magnitude of these peaks for the experimental data is chopped off. If the experimental results were extrapolated, the model's first peak of sternum acceleration would match the experimental results. The second peak of sternum acceleration for the model is lower due to the inherent stiffness of the model. The long-term behavior of the model's sternum acceleration results seems to be approaching zero as the experimental results. For this test case as in the previous test case, discrepancies noted in the sternum acceleration propagate to the velocity and displacement experimental results due to the numerical integration techniques used for obtaining velocity and displacement results. The experimental and model results for velocity and displacement are shown in Figures 34 and 35 respectively.

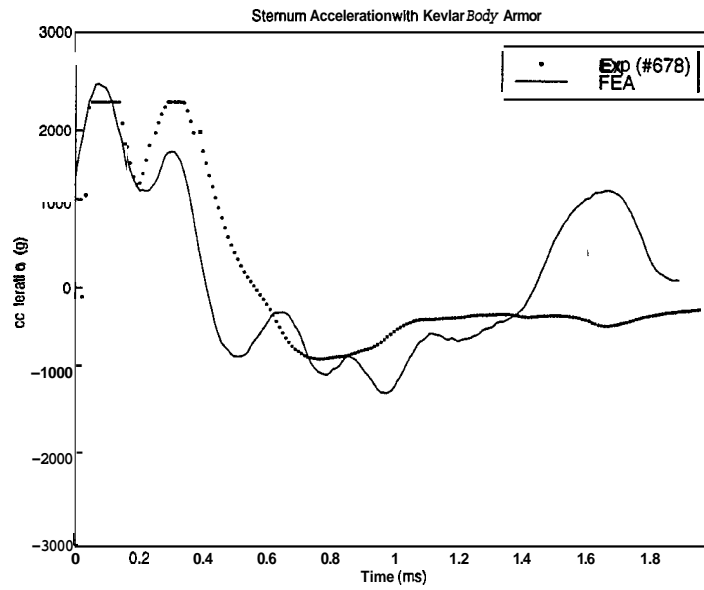


Figure 33. Sternum Acceleration (Kevlar). After Ref. [13].

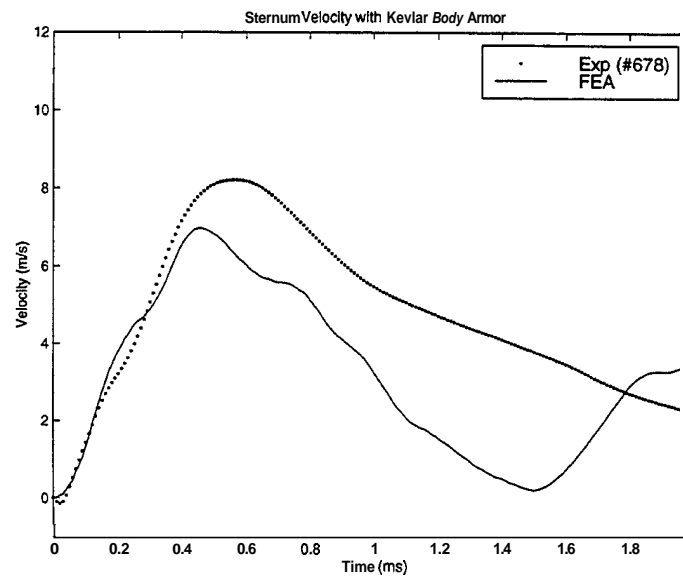


Figure 34. Sternum Velocity (Kevlar). After Ref. [13].

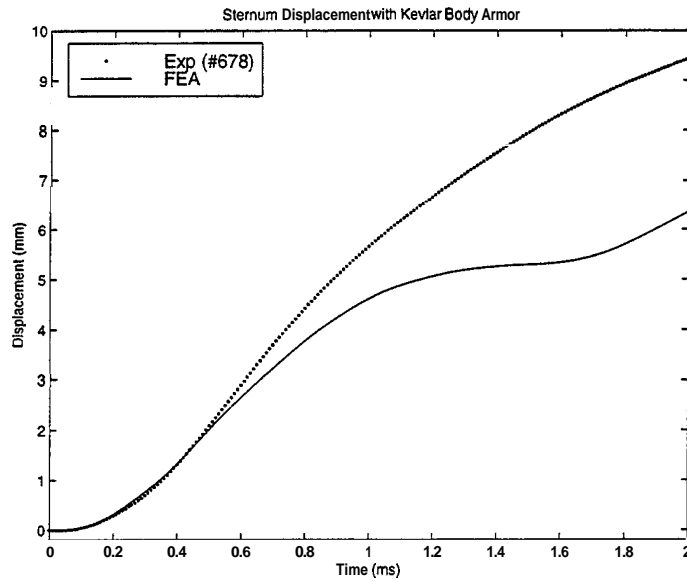


Figure 35. Sternum Displacement (Kevlar). After Ref. [13].

Comparing the model's spinal acceleration, velocity, and displacement results to the experimental results, there are significant deviations as shown in Figures 36 - 38. Examining the experimental results for the spinal acceleration, as depicted in Figure 36, shows that the spine experiences small acceleration from the bullet impact, which seems illogical. Looking at the sternum's acceleration, it would be expected that the force imposed on the sternum by the projectile impact would propagate through the body and cause significant acceleration to the spine due to the sternum reaching a peak acceleration of 2000 g. A possible cause for the low spinal acceleration is the manner the cadavers are supported during projectile impact testing. The cadavers are supported to a wooden board by wrapping a wire around the body and wooden board. Upon projectile impact, there could have been movement of the cadaver. Demaio, et al [Ref 13] noted that there was cadaver movement of two of the specimens. However the two specimens are not specified. This movement of the cadaver would impose boundary conditions that are

different from the boundary conditions used for the model resulting in the discrepancies. The movement of the cadaver would have a pronounced effect on the spinal acceleration vice the sternum acceleration due to the wooden board limiting the movement of the spine. Another possible cause for the discrepancy between the model's and experimental spinal acceleration results is instrumentation error. Demaio, et al [Ref 13] stated that the accelerometers used for the impact testing were not designed for very rapid acceleration or ballistic impact. Due to these possible causes for the discrepancies in the spinal acceleration results, there is no reason to question the viability of the model. Comparing the model's spinal acceleration results in Figure 36 to model's spinal acceleration results with the Kevlar and Boron Carbide plate body armor system in Figure 26, the trend of the spinal acceleration for both test cases is consistent. Comparing the trend of the model's (Kevlar body armor) results, Figure 36, to the experimental results of the spinal acceleration of the cadaver with the Kevlar and Boron Carbide plate body armor system in Figure 26, the trend of that experimental data correlates with the model's (Kevlar body armor) results. This shows that the model performed consistently and points to the movement of the cadaver and instrumentation error as the reason for the discrepancies between the model's and experimental results.

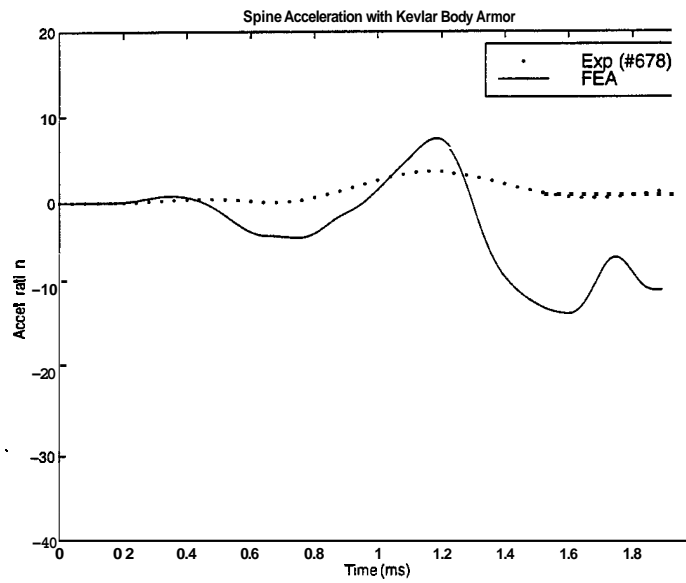


Figure 36. Spinal Acceleration (Kevlar). After Ref. [13].

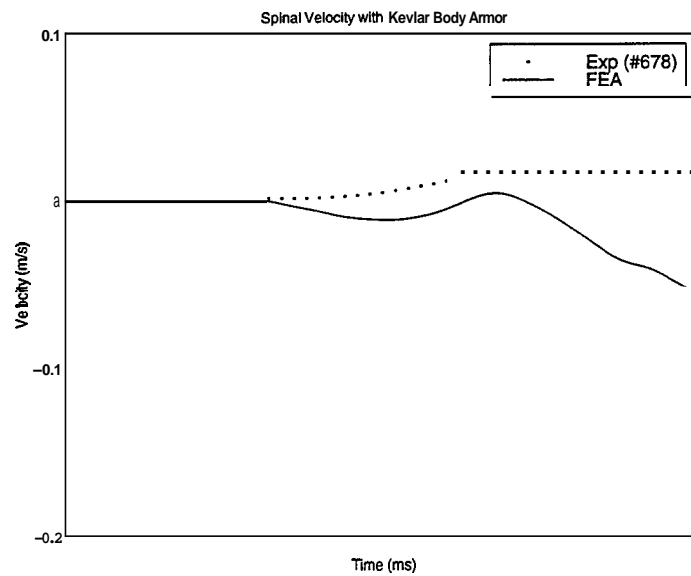


Figure 37. Spinal Velocity (Kevlar). After Ref. [13].

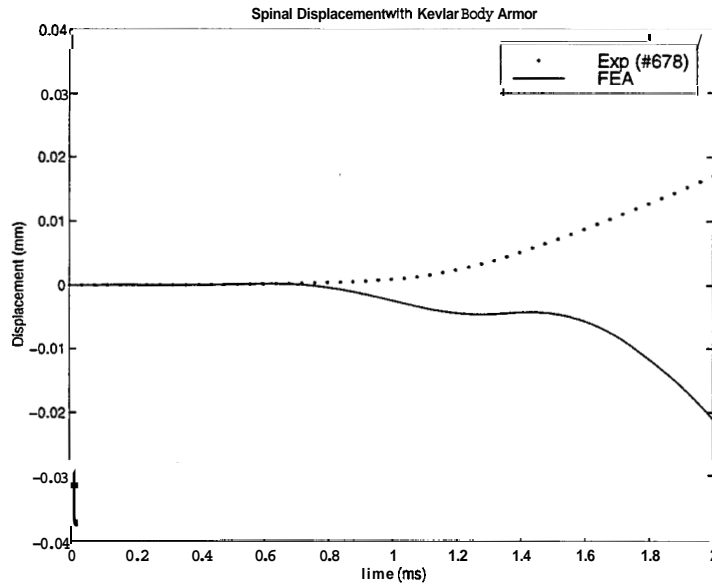


Figure 38. Spinal Displacement (Kevlar). After Ref. [13].

The acceleration, velocity, and displacement of the sternum and spine of this model compared to Jolly's [Ref. 12] model show that these parameters have the same trends. However, the magnitudes of the results for this model is slightly lower compared to Jolly's model. The lower magnitudes are due to the overall stiffness of the model increasing due to the modeling of the organs.

A comparison of the model's results to the experiment results for the pulmonary acceleration shows there are some discrepancies between these results as shown in Figure 39. The experimental results for the pulmonary acceleration show the acceleration being essentially constant at 10 g. This behavior of the pulmonary artery does not seem plausible. With the sternum being accelerated up to 2000 g, the force transmitted to the pulmonary artery would cause the acceleration of the pulmonary artery to be increasing instead of the acceleration being constant. Also the magnitude of the acceleration of the pulmonary artery would be expected to be higher than 10g. Examining the experimental



results for the Kevlar and Boron Carbide plate body armor case for the sternum acceleration and pulmonary acceleration, Figures 22 and 29, the sternum is accelerated at a lower magnitude and the pulmonary acceleration is increasing and a lot higher in magnitude compared to this test case. For the experimental testing of the cadavers, the circulatory system is pressurized up to 100 torrs. Demaio, et al [Ref. 13] states that the low acceleration of the pulmonary artery is caused due to lack of volume of heart and great vessels from the pressure not being maintained in the circulatory system. This lack of pressure possibly reduced the stiffness of the pulmonary artery, which resulted in the low acceleration of the pulmonary artery.

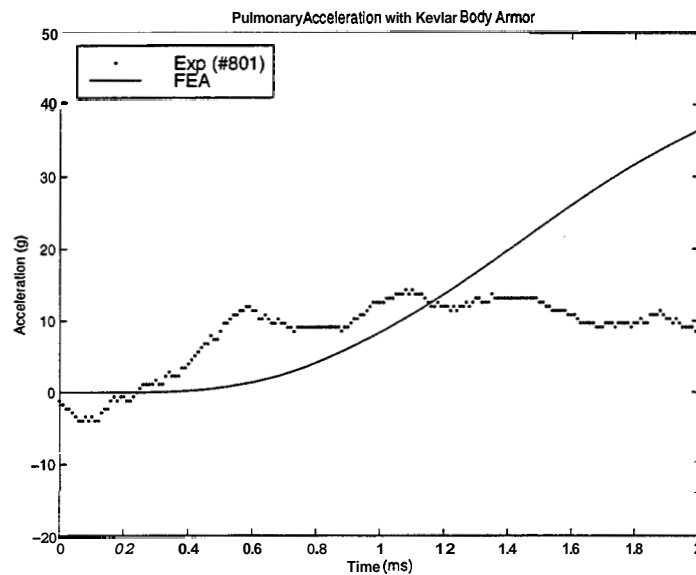


Figure 39. Pulmonary Acceleration (Kevlar). After Ref. [13].

The experimental results for ventricle pressure compared to the model have some discrepancies. The trend of the ventricle pressure correlated between the experimental and model's results as depicted in Figure 40. The magnitude of the ventricle pressure for the model is higher compared to the ventricle pressure of the experimental results. The

possible cause is due to the lack of volume of the heart from the pressure not being maintained in the circulatory system. The lack of pressure in the circulatory system reduces the stiffness of the heart causing the ventricle pressure to be lower compared to the model's results. Also another possible cause for the differences in the magnitude of the ventricle pressure for the experimental and model's results is the location where the ventricle pressure is monitored. As shown in the previous case, the location of where the ventricle pressure is monitored is a significant factor.

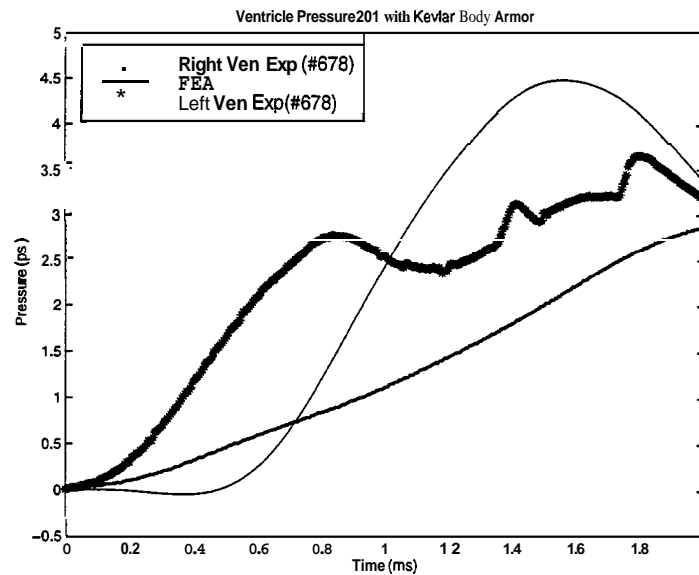


Figure 40. Ventricle Pressure (Kevlar). After Ref. [13].

Even though there are some discrepancies between the experimental and the model's results for the recorded parameters, the model is deemed viable. The discrepancies between the model and the experimental results were caused by experimental conditions that are not replicated in the model such as movement of the

cadaver during bullet impact. The behavior of the model is also consistent for both test cases.

## **B. PARAMETRIC STUDY**

A parametric study is conducted to determine the essential components of the model. The parametric study is also performed to determine the effect of varying a component has on the overall behavior of the model. The parameters that are varied are the Young's Modulus of the trachea, pulmonary arteries, and pericardium and the properties of the spring and damper elements. Each parameter was changed individually and the behavior of the model is compared to the Kevlar and Boron Carbide plate body armor case presented in the viability study. The velocity and displacement of the spine and sternum are not used for comparison due to the velocity and displacement being obtained by numerical integration of the acceleration. In the figures dealing with the parametric study, the experimental results obtained by DeMaio, et al, [Ref. 13], the results obtained previously from the model with the Kevlar and Boron Carbide plate body armor (Base Case), and the results for the model with a parameter changed are plotted (Parametric Case).

From the parametric study, the springs between the ribs and lungs and the springs between the heart and sternum and the Young's Modulus of the pericardium are the most important factors in determining the correct behavior of the model. The springs between the heart and lungs affect the overall behavior of the model but not as significantly. Changing the Young's Modulus for any other tissue had localized effects only. When the

Young's Modulus was varied for a tissue, the behavior of that tissue is affected only. The overall behavior of the model is also affected minimally.

Varying the stiffness of the springs between the ribs and lungs and the sternum and heart affects the spinal, sternum, pulmonary and pulmonary accelerations. When the stiffness of the spring elements is decreased by a factor of ten, the pulmonary acceleration and the ventricle pressures decrease due to the force transmitted by the springs from the ribs and the sternum from the bullet impact is lower due to lower stiffness of the springs as shown respectively in Figures 41, 42, and 43. However the spinal and sternum accelerations increase because the overall stiffness of the model is reduced as depicted in Figures 44 and 45.

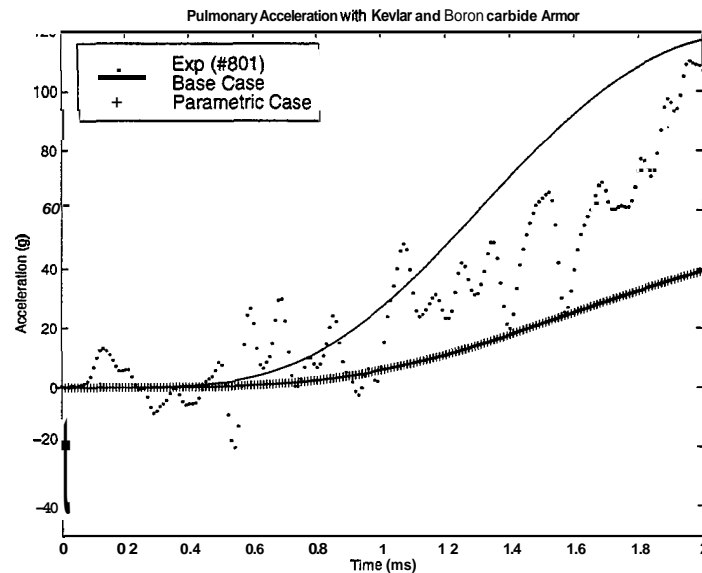


Figure 41. Pulmonary Acceleration (Kevlar and Boron Carbide Armor with Stiffness of Springs Decreased by a Factor of 10). After Ref. [13].

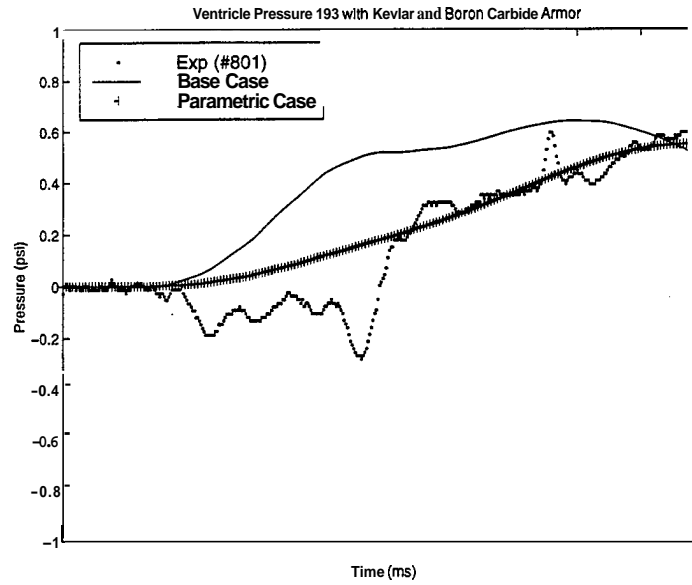


Figure 42. Ventricle Pressure Element 193 (Kevlar and Boron Carbide Armor with Stiffness of Springs Decreased by a Factor of 10). After Ref. [13].

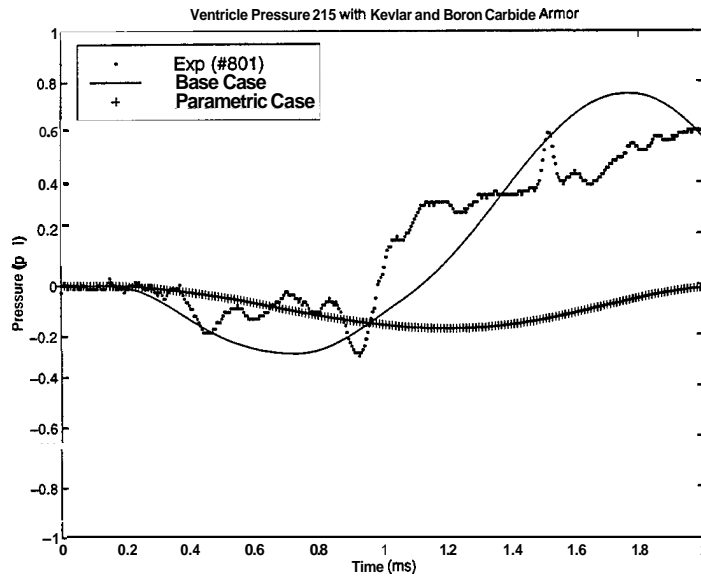


Figure 43. Ventricle Pressure Element 215 (Kevlar and Boron Carbide Armor with Stiffness of Springs Decreased by a Factor of 10). After Ref. [13].

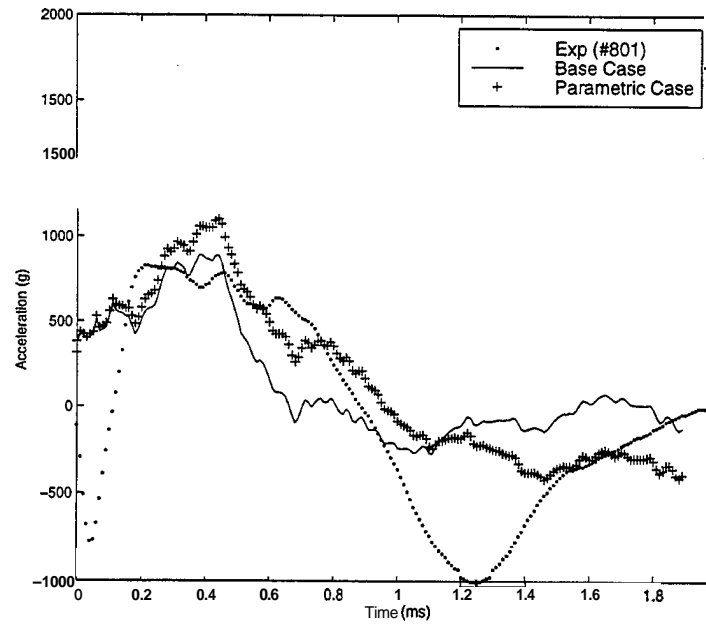


Figure 44. Sternum Acceleration (Kevlar and Boron Carbide Armor with Stiffness of Springs Decreased by a Factor of 10). After Ref. [13].

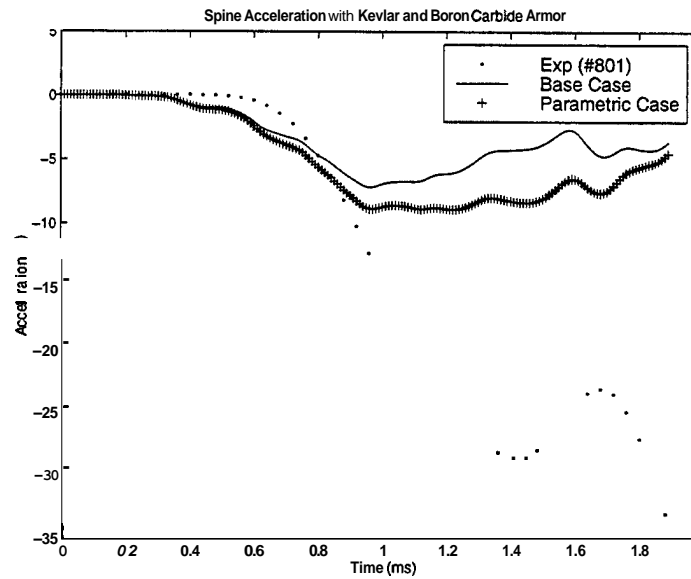


Figure 45. Spinal Acceleration (Kevlar and Boron Carbide Armor with Stiffness of Springs Decreased by a Factor of 10). After Ref. [13].

Increasing the stiffness of the spring elements by a factor of 10 between the lungs and ribs and the sternum and heart had the opposite effects on the model. The pulmonary acceleration and ventricle pressure increase due to the force transmitted by the springs from the ribs and the sternum from the bullet impact is increased due to higher stiffness of the springs as shown in Figures 46, 47, and 48. The sternum and spinal accelerations decrease due to the overall stiffness of the model increasing from the increased stiffness of the springs as illustrated in Figures 49 and 50.

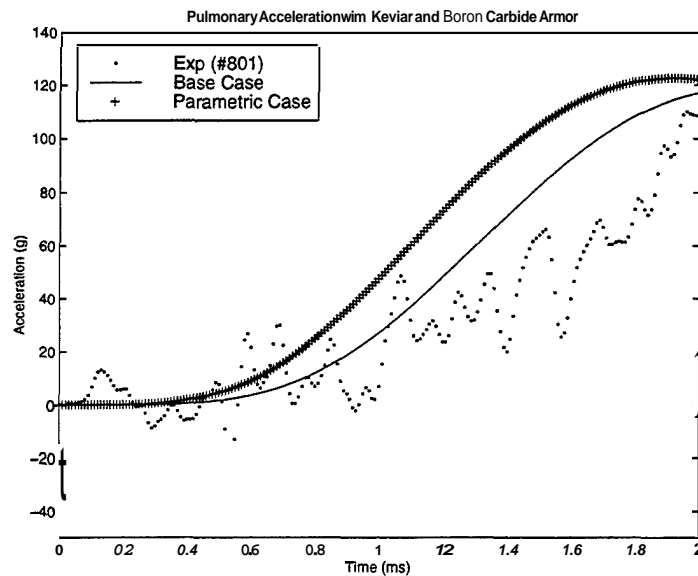


Figure 46. Pulmonary Acceleration (Kevlar and Boron Carbide Armor with Stiffness of Springs Increased by a Factor of 10). After Ref. [13].

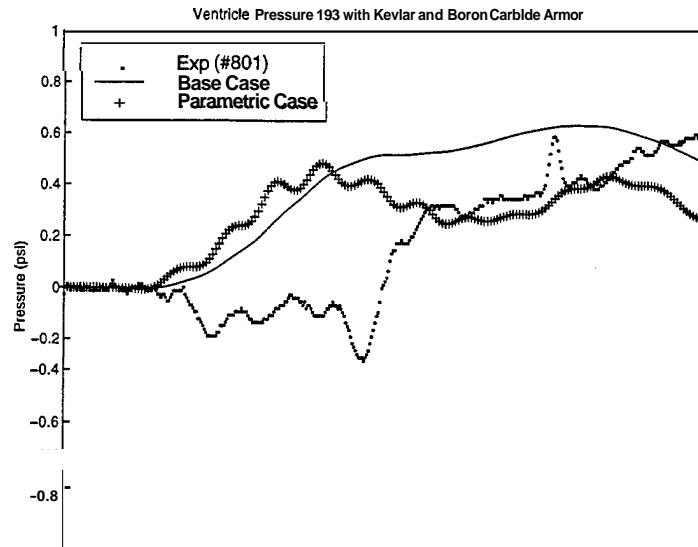


Figure 47. Ventricle Pressure Element 193 (Kevlar and Boron Carbide Armor with Stiffness of Springs Increased by a Factor of 10). After Ref. [13].

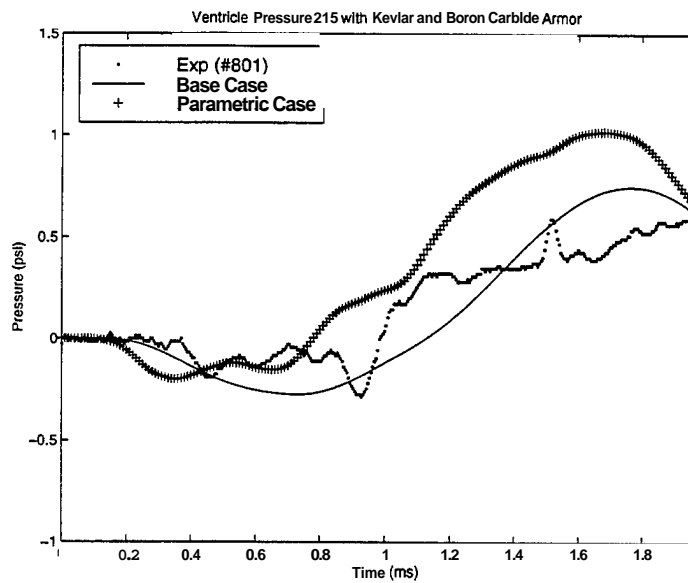


Figure 48. Ventricle Pressure Element 215 (Kevlar and Boron Carbide Armor with Stiffness of Springs Increased by a Factor of 10). After Ref. [13].



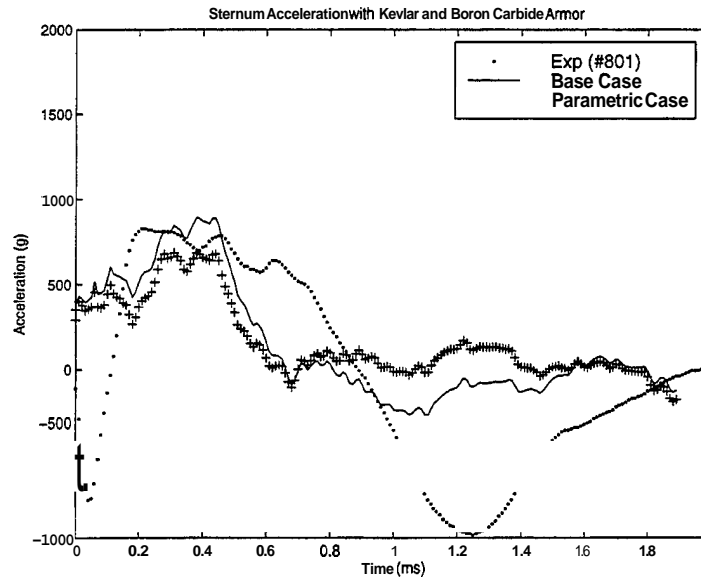


Figure 49. Sternum Acceleration (Kevlar and Boron Carbide Armor with Stiffness of Springs Increased by a Factor of 10). After Ref. [13].

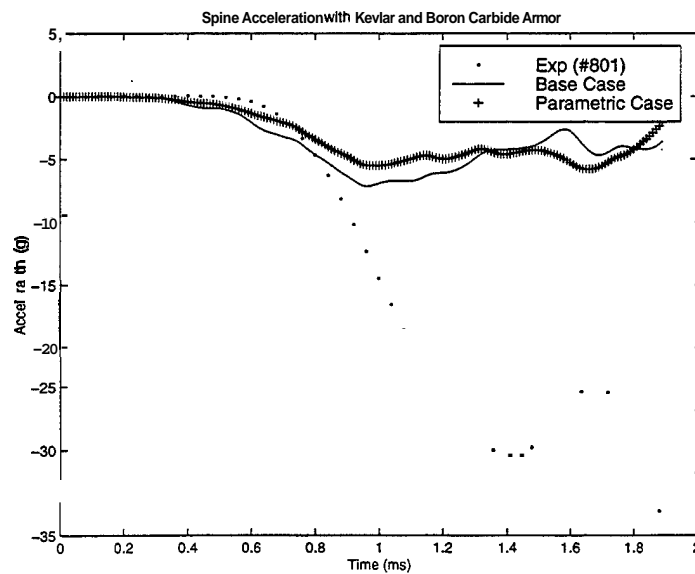


Figure 50. Spinal Acceleration (Kevlar and Boron Carbide Armor with Stiffness of Springs Increased by a Factor of 10). After Ref. [13].

Changing Young's Modulus of the pericardium affects the sternum, spinal, and pulmonary accelerations and the ventricle pressure. When the Young's Modulus is reduced by a factor of 10 from its original value, the sternum and spinal accelerations have the same trend as the Base Case. However, the magnitude of the sternum and spinal accelerations increase as shown in Figures 51 and 52 respectively. The cause for the increase in the magnitude of the acceleration is that reducing Young's Modulus of the pericardium reduced the overall inherent stiffness of the model. The pulmonary artery acceleration displays the same trend also compared to the Base Case but the magnitude of the acceleration is reduced when Young's Modulus of the pericardium is reduced by a factor of 10 as shown in Figure 53. The pulmonary artery acceleration is reduced due to the lowered stiffness of the pericardium. The stiffness of the pericardium is a function of Young's Modulus. The lowered stiffness of the pericardium allows less force to be transmitted to the pulmonary artery, which is directly attached to the heart. The ventricle pressures show deviations from the Base Case as shown in Figures 54 and 55 when Young's Modulus was reduced. The reduction in Young's Modulus affects the interaction between the pericardium, heart and blood in the heart. Increasing the modulus of elasticity of the pericardium by a factor of 10 had the opposite effect of decreasing Young's Modulus. The sternum and spinal accelerations have the same trend as the Base Case. However, the magnitude of their accelerations is reduced as shown in Figures 56 and 57 respectively. The overall inherent stiffness of the model increases with Young's Modulus being increased, which led to the lower accelerations of the sternum and spine. The pulmonary artery also displays the same trend as the Base Case but the magnitude of the acceleration increased as shown in Figure 58. The increased acceleration of the

pulmonary artery is due to the increased stiffness of the pericardium. The pericardium and the heart will transmit more force to the pulmonary artery. The ventricle pressure as depicted in Figures 59 and 60 show deviations from the Base Case due to the change of the interaction between the pericardium, heart, and blood.

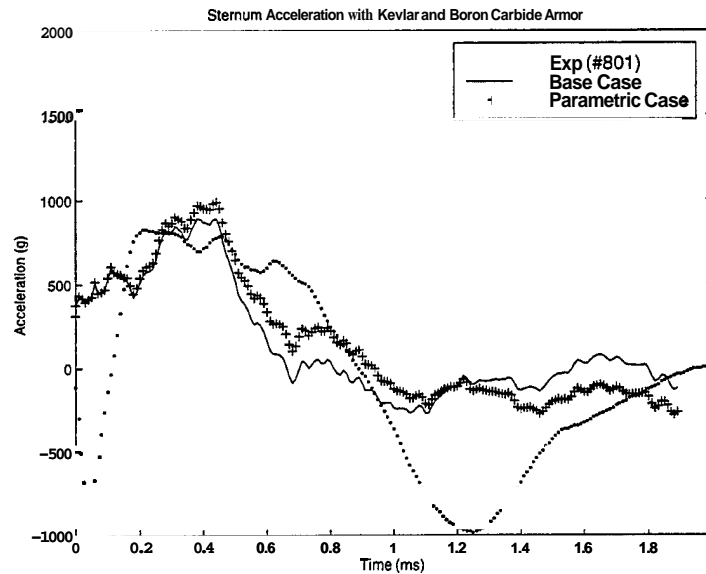


Figure 51. Sternum Acceleration (Kevlar and Boron Carbide Armor with Young's Modulus of Pericardium Decreased by a Factor of 10). After Ref. [13].

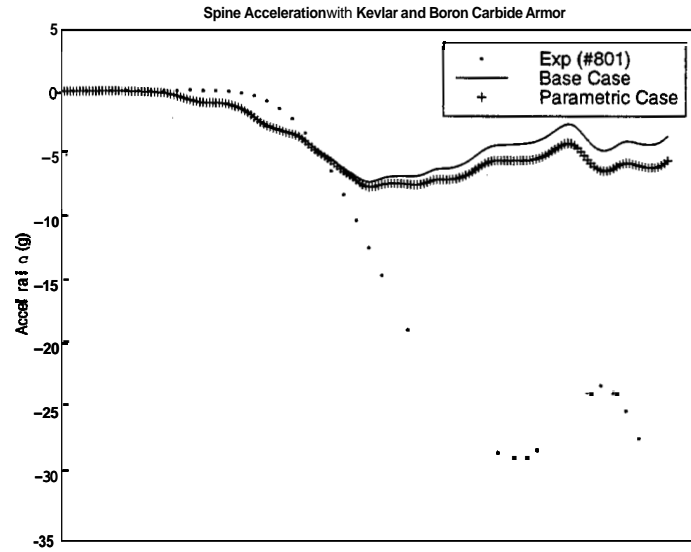


Figure 52. Spinal Acceleration (Kevlar and Boron Carbide Armor with Young's Modulus of Pericardium Decreased by a Factor of 10). After Ref. [13].

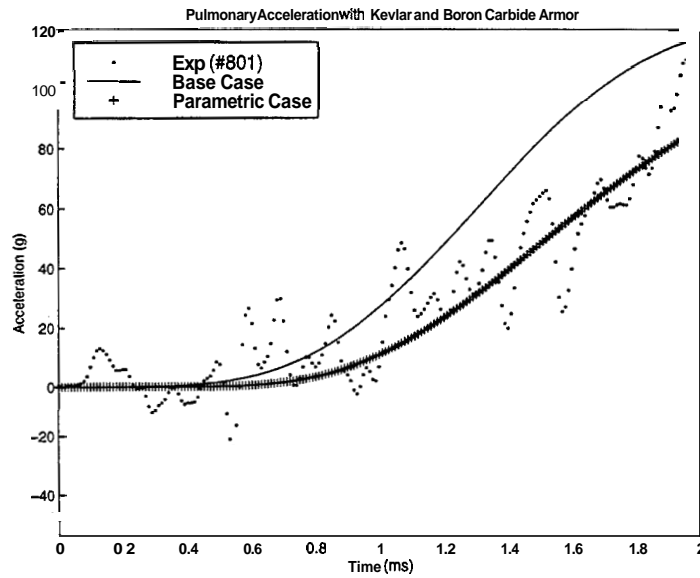


Figure 53. Pulmonary Artery Acceleration (Kevlar and Boron Carbide Armor with Young's Modulus of Pericardium Decreased by a Factor of 10). After Ref. [13].

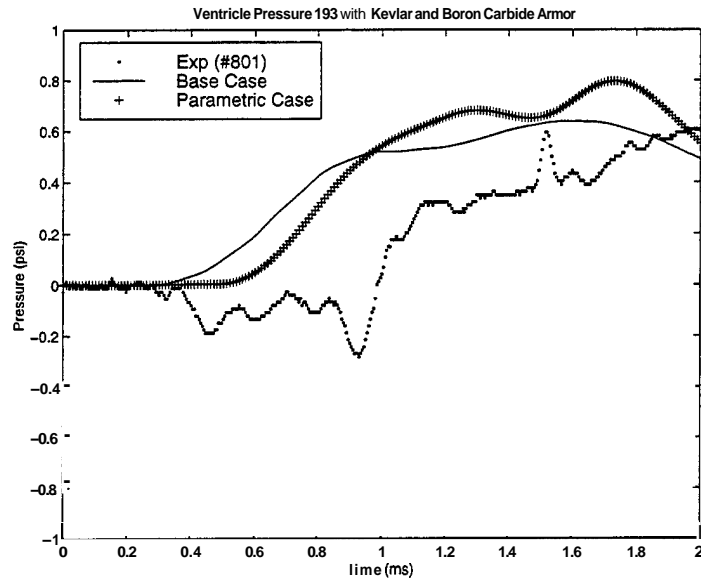


Figure 54. Ventricle Pressure Element 193 (Kevlar and Boron Carbide Armor with Young's Modulus of Pericardium Decreased by a Factor of 10). After Ref. [13].

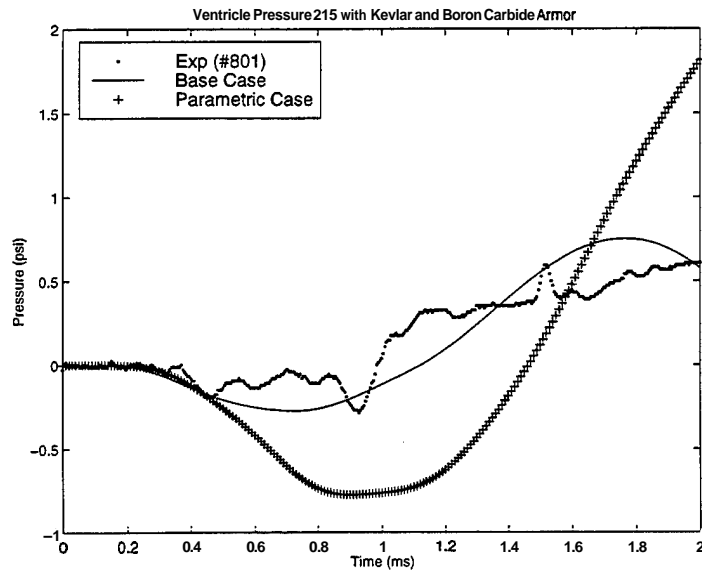


Figure 55. Ventricle Pressure Element 215 (Kevlar and Boron Carbide Armor with Young's Modulus of Pericardium Decreased by a Factor of 10). After Ref. [13].

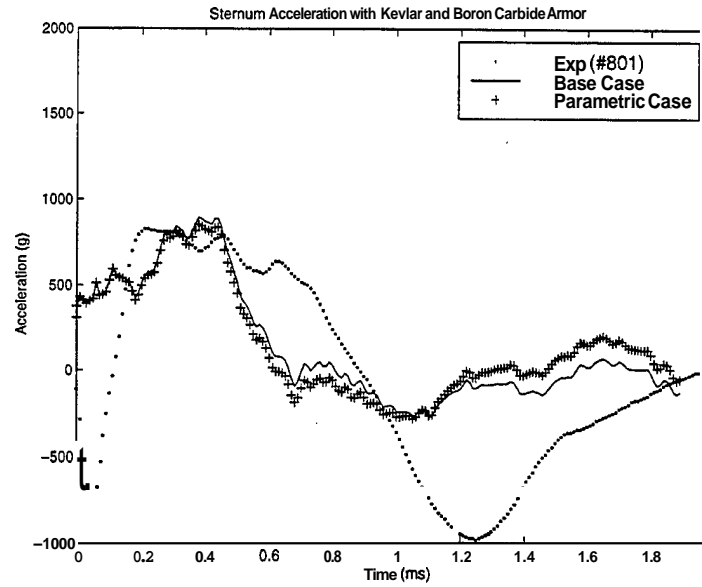


Figure 56. Sternum Acceleration (Kevlar and Boron Carbide Armor with Young's Modulus of Pericardium Increased by a Factor of 10). After Ref. [13].

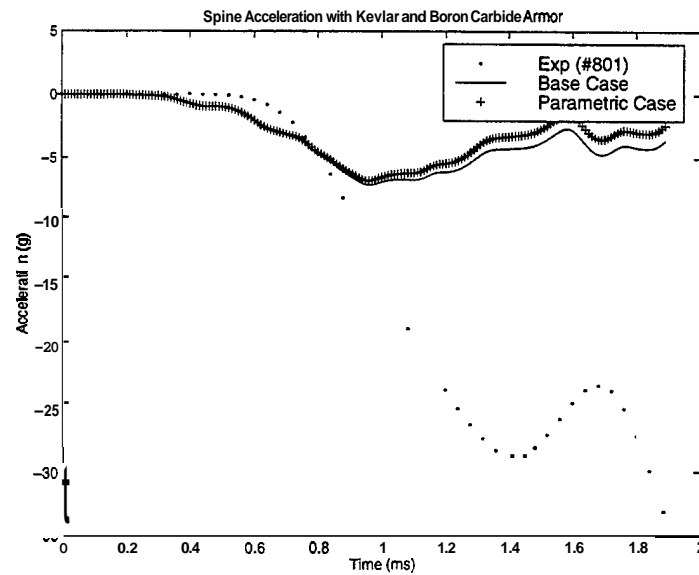


Figure 57. Spinal Acceleration (Kevlar and Boron Carbide Armor with Young's Modulus of Pericardium Increased by a Factor of 10). After Ref. [13].

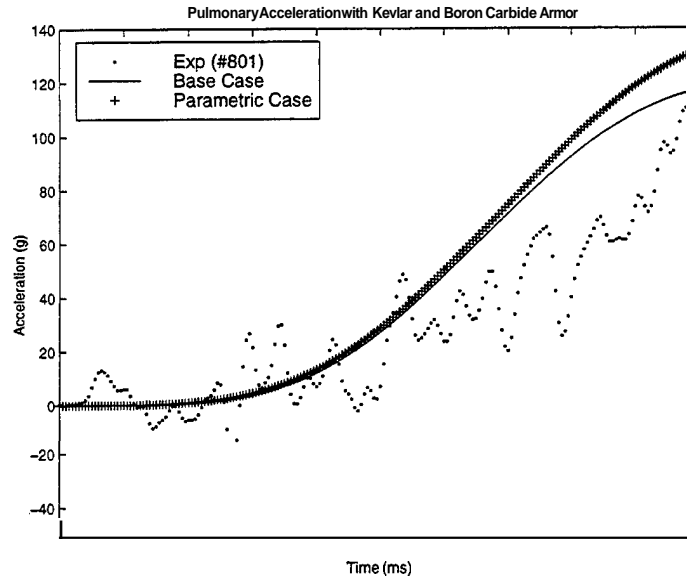


Figure 58. Pulmonary Artery Acceleration (Kevlar and Boron Carbide Armor with Young's Modulus of Pericardium Increased by a Factor of 10). After Ref. [13].

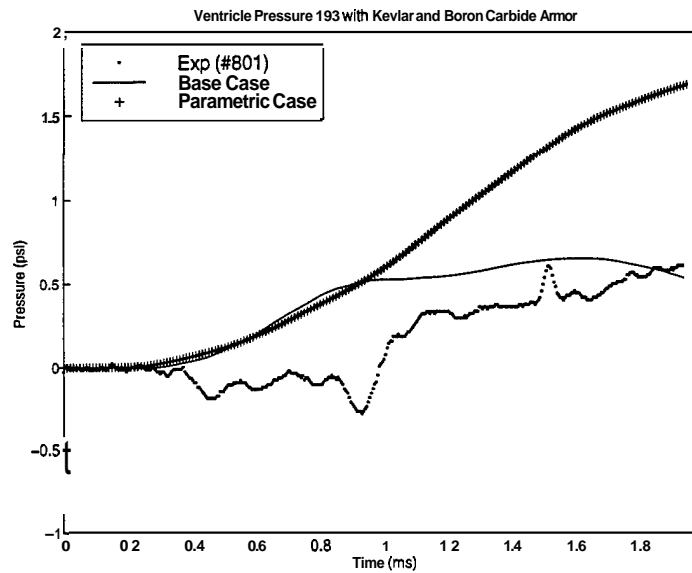


Figure 59. Ventricle Pressure Element 193 (Kevlar and Boron Carbide Armor with Young's Modulus of Pericardium Increased by a Factor of 10). After Ref. [13].

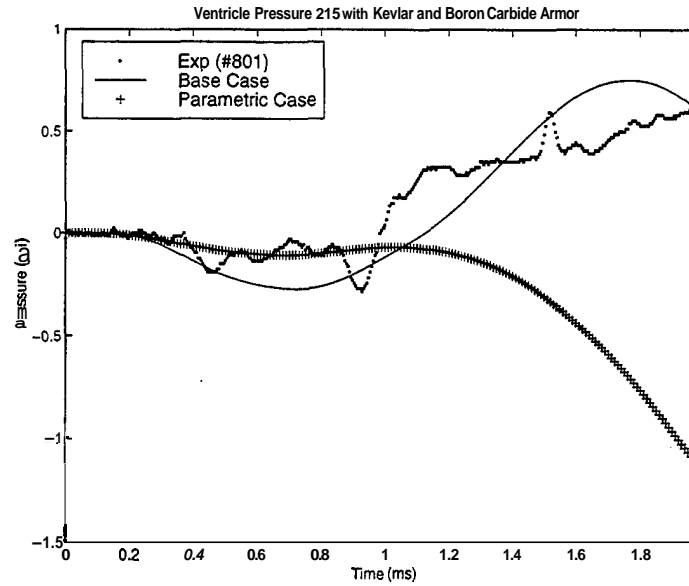


Figure 60. Ventricle Pressure Element 215 (Kevlar and Boron Carbide Armor with Young's Modulus of Pericardium Increased by a Factor of 10). After Ref. [13].

Modifying the stiffness of the spring elements between the heart and lungs affects the spinal and pulmonary acceleration and ventricle pressure. When the stiffness of the spring elements is decreased by a factor of ten from its original value, the magnitude of the spinal and pulmonary artery accelerations and ventricle pressure starts to increase at 1msec and keeps increasing to the end of the analysis as shown respectively in Figure 61, 62, 63, and 64. When the stiffness of the springs is increased by a factor of 10, the opposite effect compared to when the spring stiffness is decreased occurs. The spinal and pulmonary accelerations start to decrease at 1msec and keep decreasing to the end of the analysis as depicted in Figure 65, 66, 67, and 68.



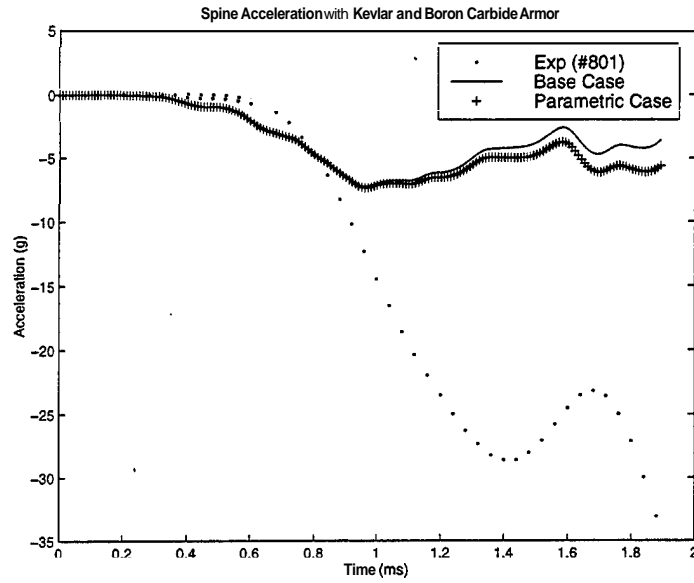


Figure 61. Spinal Acceleration (Kevlar and Boron Carbide Armor with Stiffness of Springs Between Heart Lungs Decreased by a Factor of 10). After Ref. [13].

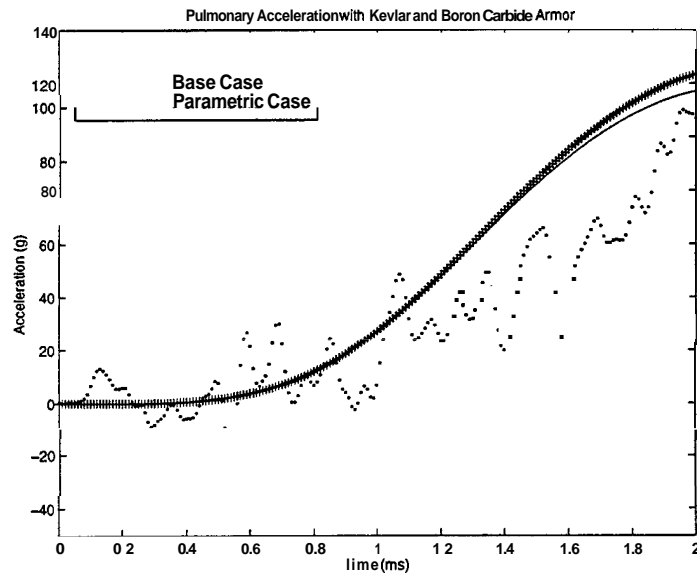


Figure 62. Pulmonary Artery Acceleration (Kevlar and Boron Carbide Armor with Stiffness of Springs Between Heart Lungs Decreased by a Factor of 10). After Ref. [13].

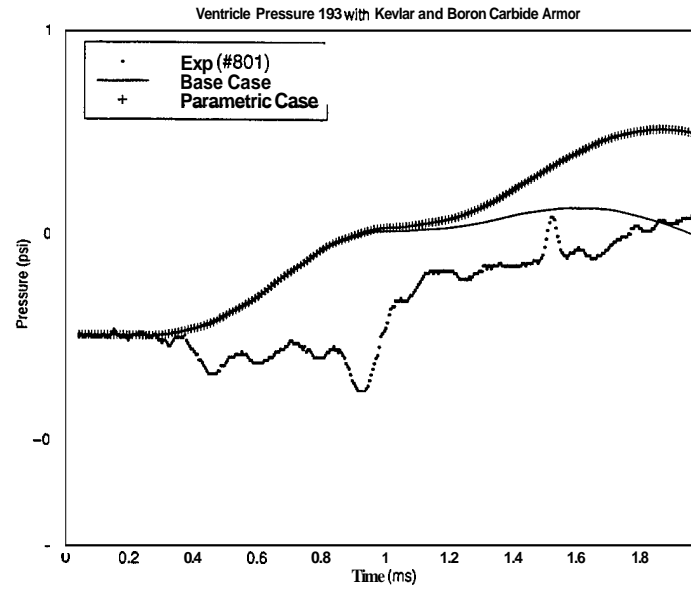


Figure 63. Ventricle Pressure Element 193 (Kevlar and Boron Carbide Armor with Stiffness of Springs Between Heart Lungs Decreased by a Factor of 10). After Ref. [13].

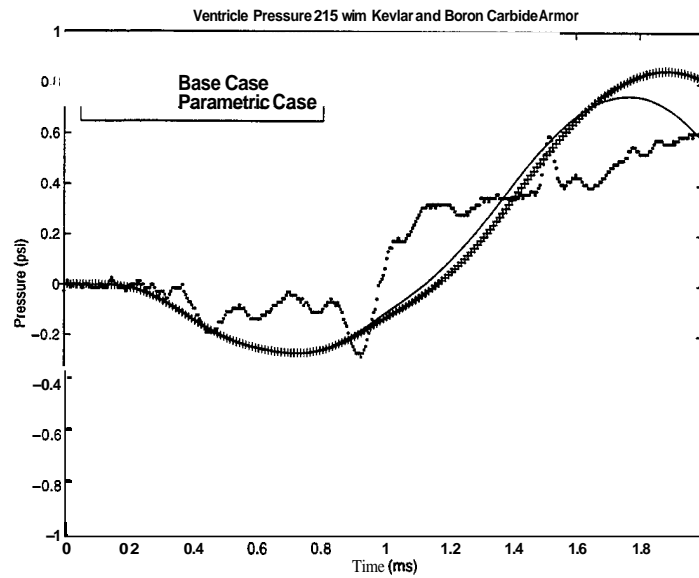


Figure 64. Ventricle Pressure Element 215 (Kevlar and Boron Carbide Armor with Stiffness of Springs Between Heart Lungs Decreased by a Factor of 10). After Ref. [13].

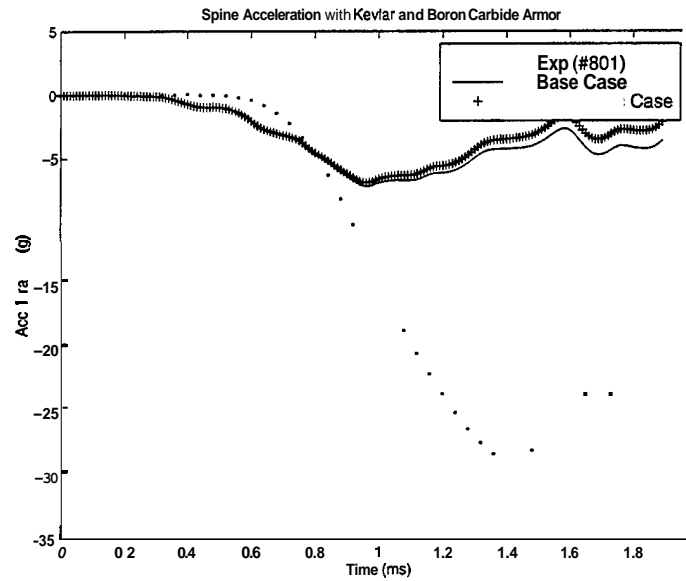


Figure 65. Spinal Acceleration (Kevlar and Boron Carbide Armor with Stiffness of Springs Between Heart Lungs Increased by a Factor of 10). After Ref. [13].

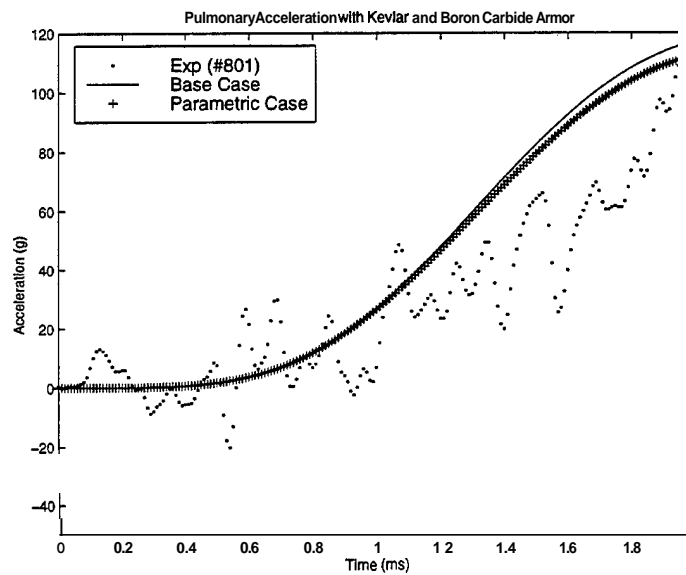


Figure 66. Pulmonary Artery Acceleration (Kevlar and Boron Carbide Armor with Stiffness of Springs Between Heart Lungs Increased by a Factor of 10). After Ref. [13].

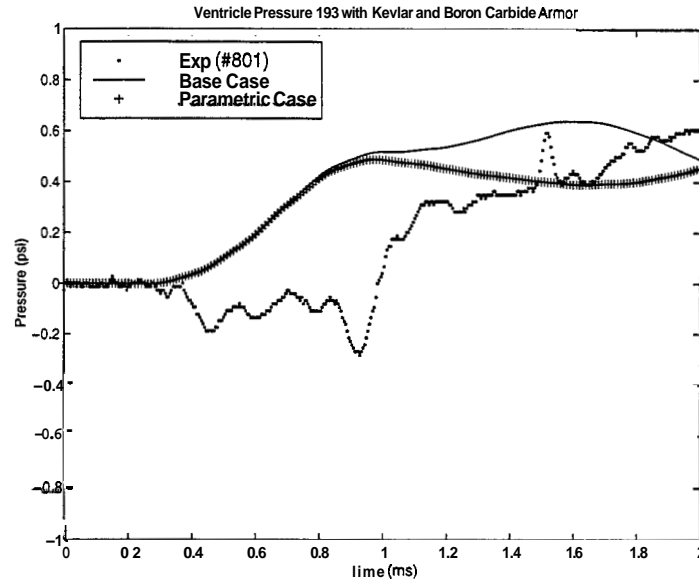


Figure 67. Ventricle Pressure Element 193 (Kevlar and Boron Carbide Armor with Stiffness of Springs Between Heart Lungs Increased by a Factor of 10). After Ref. [13].

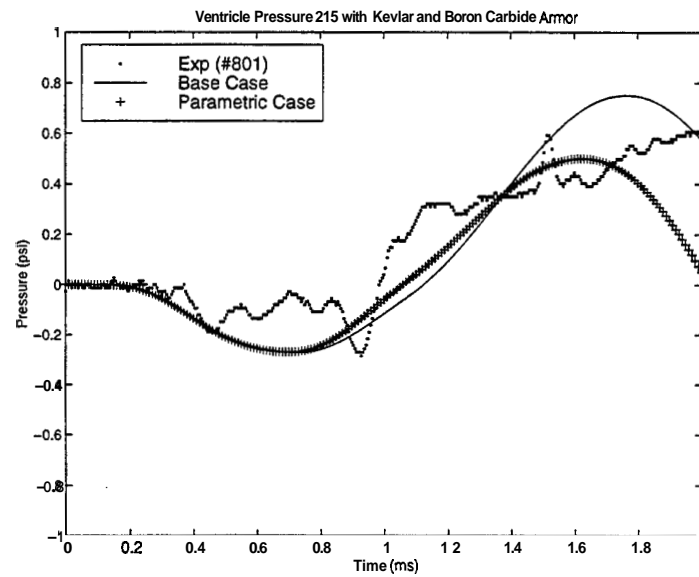


Figure 68. Ventricle Pressure Element 215 (Kevlar and Boron Carbide Armor with Stiffness of Springs Between Heart Lungs Increased by a Factor of 10). After Ref. [13].

When Young's Modulus of the trachea and pulmonary artery are varied individually, the behavior of the soft tissue that has its Young's Modulus varied is affected only. There are no noticeable changes in the other recorded parameters of the model. The frequency and magnitude of the acceleration of the trachea and pulmonary artery increase when their Young's Moduli is increased by a factor of ten from its original value as illustrated in Figures 69 and 70, respectively. The increase in the Young's Modulus leads to an increase in the speed of sound calculated for the model according to the equation listed below:

$$v_s = \sqrt{\frac{E}{\rho}}$$

$v_s$  - Speed of Sound

$E$  – Young's Modulus

$\rho$  - Density

The increase in the speed of sound results in the increase in frequency response for the trachea and pulmonary artery. The stiffness of the trachea and pulmonary artery is a function of Young's Modulus. With Young's Modulus being increased, the stiffness of the trachea and pulmonary artery increases, which leads to the higher acceleration of each tissue. The opposite effect occurs to the trachea and pulmonary artery when the Young's Modulus is decreased by a factor of ten. The frequency and magnitude of the acceleration decrease for the trachea and pulmonary artery as shown in Figures 71 and 72. The frequency decreases due to the decrease in the speed of sound for the model from the reduced Young's Modulus. The acceleration also decreases due to the lower stiffness from the reduced Young's Modulus.

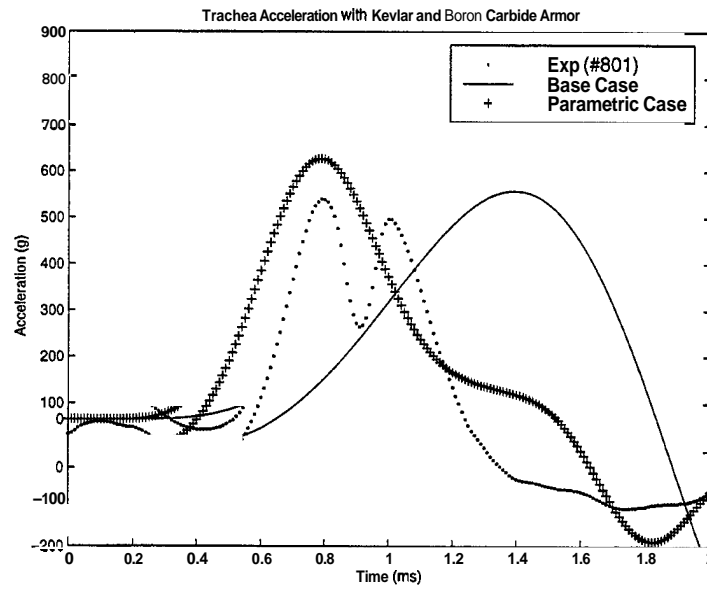


Figure 69. Trachea Acceleration (Kevlar and Boron Carbide Armor with Young's Modulus of Trachea Increased by a Factor of 10). After Ref. [13].

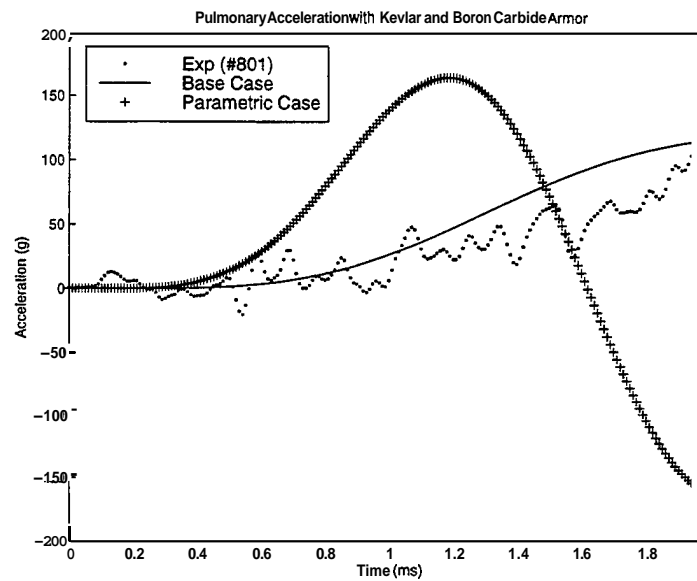


Figure 70. Pulmonary Artery Acceleration (Kevlar and Boron Carbide Armor with Young's Modulus of Pulmonary Artery Increased by a Factor of 10). After Ref. [13].

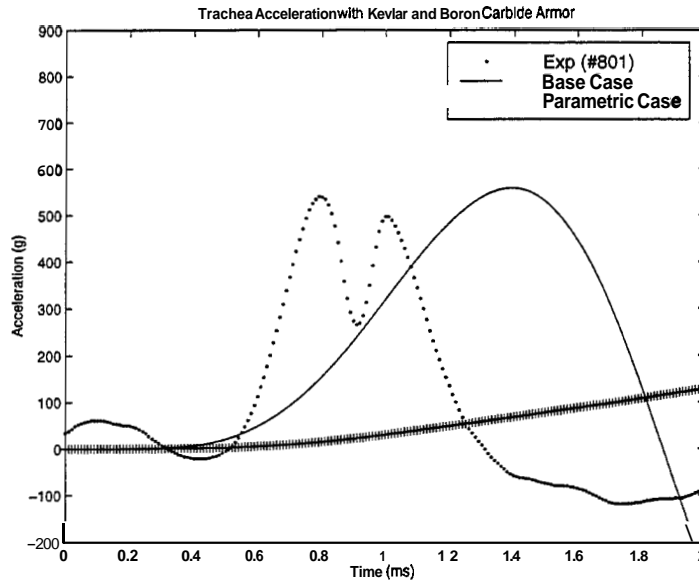


Figure 71. Trachea Acceleration (Kevlar and Boron Carbide Armor with Young's Modulus of Trachea Decreased by a Factor of 10). After Ref. [13].

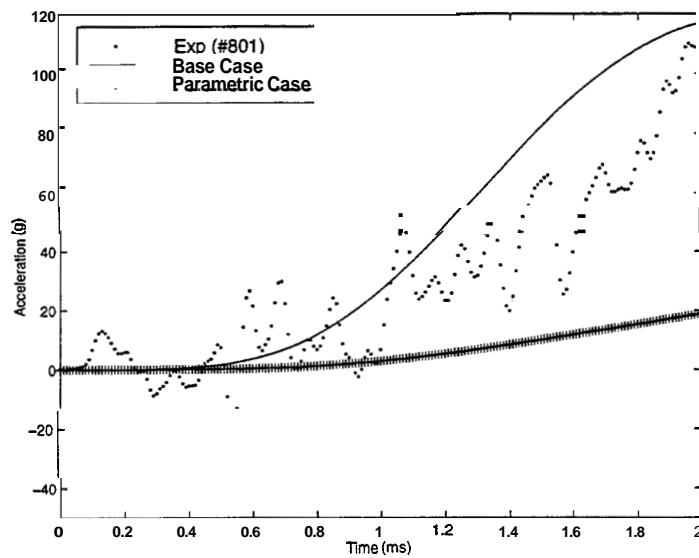


Figure 72. Pulmonary Artery Acceleration (Kevlar and Boron Carbide Armor with Young's Modulus of Pulmonary Artery Decreased by a Factor of 10). After Ref. [13].

Removing the dampers between the ribs and lungs and the heart and sternum had no noticeable effects on the behavior of the model. Increasing the damping by a factor of 10 from its original value between the ribs and lungs and the heart and sternum had no noticeable effect on the behavior of the model. Furthermore, removing the dampers or increasing the damping between the heart and lungs had no noticeable effects.



## **IV. CONCLUSIONS AND RECOMMENDATIONS**

### **A. CONCLUSIONS**

The purpose of this study was to develop a finite element model of the human thorax with a body armor system to adequately determine the biodynamical response of the thorax from a projectile impact. The biodynamical response of the thorax was examined under two different scenarios. The first scenario studied the biodynamical response of the human thorax with a body armor consisting of Kevlar and Boron Carbide plate struck by a NATO 7.62 mm M80 ball round. The second scenario studied the biodynamical response of the human thorax with a body armor consisting of Kevlar only being struck by a NATO 9mm full metal jacket round. The finite element model of the human thorax included the thoracic skeleton, heart, lungs, major veins, trachea, and bronchi. The finite element model was deemed to be viable by the comparison of the results of the model to the experimental results obtained from firing tests conducted on cadavers for the two different scenarios. The parameters that were used for comparison between the experimental and the model's results were the acceleration of the sternum, spine, pulmonary artery, and trachea and ventricle pressure. After the model was found to be viable, a parametric study was performed to determine the critical components of the finite element model. The parametric study determined that the spring elements between the ribs and lungs and heart and sternum were the most important component of the model. The spring elements were necessary to transmit the force of the bullet impact to the internal organs in the thorax. The addition of the spring elements also increased the overall inherent stiffness of the model. The magnitude of the acceleration for spine and sternum in comparison to Jolly's [Ref. 12] model were lower due to the increased

stiffness of the model. Additional components of the model that were found to significantly affect the overall behavior of the model were Young's Modulus of the pericardium, and the spring elements between the heart and lung.

## **B. RECOMMENDATIONS**

Even though the model provides adequate results, several refinements can be made.

- The acceleration of the sternum, spine, trachea, and pulmonary artery and ventricle pressure varies on where the accelerometers and pressure transducers are mounted on the cadavers. To get an accurate comparison between the model and experimental results, the exact location of where the instrumentation is mounted to the cadaver needs to be known.
- More research conducted into the material properties of the human body. There is inadequate data available on the material properties of the human body. Also the information that is available on the material properties of the body is based on static testing not on dynamic testing.
- The model lacks the detailed description of the heart. The heart should be broken into its four chambers to determine if there is a significant difference between the right and left ventricle pressure measured by the model. *Also* the model should include additional soft tissues of the thorax such as the diaphragm to determine their effect on the overall behavior of the model.

## LIST OF REFERENCES

1. Best, C. H. and Taylor, N. B. *The Human Body: Its Anatomy and Physiology*, 4<sup>th</sup> Ed., Holt, Rinehart, & Winston, 1963.
2. Gray, H., *Anatomy: Descriptive and Surgical*, 15<sup>th</sup> ed., Barnes and Noble Books, 1995.
3. Roberts, S. B. and Chen, P. H., "Elastostatic Analysis of the Human Thoracic Skeleton," *Journal of Biomechanics*, v. 3, pp. 527-545, 1970.
4. Andriacchi, T., Shultz, A., Belytschko, T., and Galante, J., "A Model for the Studies of the Mechanical Interaction between the Human Spine and Rib Cage," *Journal of Biomechanics*, v. 10, pp. 497-507, 1974.
5. Sundaram, S., and Feng, C., "Finite Element Analysis of the Human Thorax," *Journal of Biomechanics*, v. 10, pp. 505-516, 1977.
6. Chen, P.H., "Finite Element Dynamic Structural Model of the Human Thorax for Chest Impact Response and Injury Studies," *Aviation Space and Environmental Medicine* 49(1): pp. 143-149, 1978.
7. Plank, G.R., Eppinger, R.H., "An Improved Finite Element Model of the Human Thorax," 12<sup>th</sup> ESV, pp. 665-672, 1991.
8. Wang, H. K., *Development of a Side Impact Finite Element Human Thoracic Model*, Doctorate Thesis, Wayne State University, Detroit, Michigan, 1995.
9. Yogananda, N. and Pintar, F., "Biomechanics of Human Thoracic Ribs," *Journal of Biomechanical Engineering*, v. 120, pp. 100-104, February 1998.
10. Yamada, H, M.D., *Strength of Biological Materials*, Williams and Wilkins, 1970
11. Hughes, T., *Biomechanical Model of the Human Thorax for Impact Analysis*, Master's Thesis, Naval Postgraduate School, Monterey, California, September 1999.
12. Jolly J. E., *Computer Modeling and Simulation of Bullet Impact to the Human Thorax*", Master's Thesis, Naval Postgraduate School, Monterey, California, June 2000.
13. DeMaio, M., Parks, S., et al., "Biomechanical Evaluation of Chest Body Armor," report, Armed Forces Institute of Pathology (AFIP).
14. Bo, W.J., Meschan, I., Krueger, W.A., "*Basic Atlas of Cross-Sectional Anatomy*", W.B. Saunders Company, 1980.

15. Fung, Y.C., *Biomechanics: Mechanical Properties of Living Tissue*, 2<sup>nd</sup> Ed., Springer-Verlag, New York, 1993.
16. Kwon, Y., and Bang, H., *The Finite Element Method Using MATLAB*, CRC Press, 1997.

## INITIAL DISTRIBUTION LIST

1.	Defense Technical Information Center ..... 8725 John J. <b>Kingman</b> Road, Suite 0944 Ft. Belvoir, VA 22060-6218	.2
2.	Dudley Knox Library ..... Naval Postgraduate School 411 Dyer Road Monterey, CA 93943-5101	2
3.	Professor Young W. Kwon <b>ME/Kw</b> ..... Department of Mechanical Engineering Naval Postgraduate School Monterey, CA 93943	2
4.	Headquarters, U.S. Army Soldier & Biological Chemical Command ..... Soldier Systems Center <b>Attn:</b> AMSSB-PM-RST-E(B) (James Mackiewicz) Kansas Street Natick, MA 01760-5021	1
5.	CDR Marlene DeMaio, MC USNR ..... Department of Orthopedic Pathology Armed Force Institute of Pathology 14 <sup>th</sup> and Alaska, NW Washington, DC 20306-6000	.2
6.	John A. Lobuono, LT, USN ..... 68 <b>Unity</b> Road Stamford, CT 06905	1
7.	Naval Engineering Curricular Office, Code 34 ..... Naval Postgraduate School Monterey, CA 93943-5000	1
8.	Research Office, Code 09 ..... Naval Postgraduate School Monterey, CA 93943	1